Electronic Supplementary Information (ESI)

Regulating Co-O Covalency to Manipulate Mechanistic Transformation for Enhancing Activity/Durability in Acidic Water Oxidation

Jiachen Zhang, [a] Guangbo Chen,[b] Dongmei Sun,[a] Yawen Tang,[a] Wei Xing,[c, d] Hanjun Sun,*[a] and Xinliang

Feng *[b,e]

[a] Jiangsu Key Laboratory of New Power Batteries, Jiangsu Collaborative Innovation Center of Biomedical Functional Materials, School of Chemistry and Materials Science, Nanjing Normal University, 210023 Nanjing, China.
E-mail: hanjun.sun@njnu.edu.cn
[b] Center for Advancing Electronics Dresden (cfaed) and Faculty of Chemistry and Food Chemistry, Technische Universität Dresden, 01062 Dresden, Germany
E-mail: xinliang.feng@tu-dresden.de
[c] State Key Laboratory of Electroanalytic Chemistry, Jilin Province Key Laboratory of Low Carbon Chemistry Power, Changchun Institute of Applied Chemistry, Chinese Academy of Sciences, 130022 Changchun, China.
[d] School of Applied Chemistry and Engineering, University of Science and Technology of China, 230026 Hefei, China.
[e] Max Planck Institute of Microstructure Physics, Halle (Saale) 06120, Germany.

Methods

Materials

Cobalt (II) acetate tetrahydrate ($Co(CH_3COO)_2 \cdot 4H_2O$) was purchased from Sigma-Aldrich. Ethylene glycol ($CH_2OH)_2$, ethanol (CH_3CH_2OH), and potassium hydroxide (KOH) were purchased from Sinopharm Chemical Reagent Co., Ltd. Polyvinylpyrrolidone (M_w = 58000) and ^{18}O Water (^{18}O, 97 %) was purchased from Shanghai Macklin Biochemical Co., Ltd. Ruthenium (III) chloride hydrate ($RuCl_3 \cdot xH_2O$) and ruthenium oxide (RuO_2, Ru ≥ 75.2%) were purchased from DB Biotechnology Co., Ltd. The commercial Pt/C (20 wt%) catalyst was supplied by Johnson Matthey. The carbon cloth was purchased from Suzhou Sinero Technology Co., Ltd.

Preparation of cobalt precursor

Typically, 0.093 mmol $Co(CH_3COO)_2 \cdot 4H_2O$ and 0.23 mmol polyvinylpyrrolidone were dispersed in 20 mL ethylene glycol under the protection of argon. Then the mixture was heated to 170 °C under the protection of argon for 3 h. After cooling to room temperature, the obtained product was collected by centrifugation, washed with ethanol, and dried under vacuum.

Preparation of pristine Co_3O_4 and Ru SAs-CoO$_x$

After the cobalt precursor was calcined at 300 °C for 10 min, the pristine Co_3O_4 was synthesized. Then 10 mg pristine Co_3O_4 and 0.075 mmol $RuCl_3 \cdot xH_2O$ were dispersed in 4 mL deionized water and stirred overnight under 60 °C. The product was washed with deionized water and dried under vacuum. Finally, the product was calcined at 300 °C for 30 min to obtain Ru SAs-CoO$_x$. Ru-CoO$_x$ catalysts with different Ru content (Ru-CoO$_x$-0.0125, Ru-CoO$_x$-0.025, Ru-CoO$_x$-0.05, Ru-CoO$_x$-0.1, and Ru-CoO$_x$-0.125) were also prepared by a similar method except that the dosage of $RuCl_3 \cdot xH_2O$ (0.0125 mmol, 0.025 mmol, 0.05 mmol, 0.1 mmol, and 0.125 mmol) was changed.

Preparation of Ni-CoO$_x$, Fe-CoO$_x$, and Mn-CoO$_x$

Ni-CoO$_x$, Fe-CoO$_x$, and Mn-CoO$_x$ catalysts were also prepared by a similar method with Ru SAs-CoO$_x$ except that the types of metal salts ($NiCl_2 \cdot 6H_2O$, $FeCl_3 \cdot 6H_2O$, and $MnCl_2 \cdot 4H_2O$) was changed.

Material characterization

The crystal structure information of the as-fabricated samples was measured by X-ray powder diffraction (XRD) on a D/max-rC X-ray diffractometer (Cu Kα radiation, λ = 1.5406 Å). TEM and HRTEM images were inquired on a JEOL JEM-2100F transmission electron microscopy manipulated with an accelerating voltage of 200 kV. Elemental mapping images and HAADF-STEM images were performed on a FEI Tecnai G2 F20 microscope, an accessory built on the JEOL JEM-2100F. N_2 adsorption/desorption isotherms were measured at 77 K with a Micromeritics ASAP 2050 system. ESR measurements were measured with a Bruker A300-10/12. The chemical composition of samples was analyzed by inductively coupled plasma atomic emission spectroscopy (ICP-AES). To ensure complete dissolution, 100 mg of sample was dissolved in a mixture of 5 mL HNO_3, 1 mL HF, 1 mL H_2O_2 and 1 ml HCl and heated under 200 °C for 8 h. X-ray photoelectron spectroscopy (XPS) was examined by on Thermo VG Scientific ESCALAB 250 spectrometer with an Al Kα light source. The X-ray absorption spectra (XAS) including X-ray absorption near-edge structure (XANES) and extended X-ray absorption fine structure (EXAFS) of the samples at Ru K-edge were collected at the Singapore Synchrotron Light Source (SSLS) center, where a pair of channel-cut Si (111) crystals were used in the monochromator. The Ru K-edge XANES data were recorded in a transmission mode. Ru foil and RuO_2 were used as references. The storage ring was working at the energy of 2.5 GeV with an average electron current of below 200 mA. The acquired EXAFS data were extracted and processed according to the standard procedures using to ATHENA module implemented in the FEFIT software packages.

Electrocatalytic OER Measurement

The OER activity in N_2-saturated 0.1 M $HClO_4$ is performed on CHI760E electrochemistry workstation via adopting a three-electrode test system. The scan rate of LSV is 5 mV s^{-1}. A glassy carbon (GC) electrode (diameter: 3 mm), calomel electrode and graphite rod were used as the working, reference and counter electrode, respectively. For electrode preparation, 5 mg of catalyst was dispersed in 1 mL deionized water by sonication for over 30 minutes. Then, 10 μL of the above suspension was drop-casted to glassy carbon electrode. After dried at room temperature, 3 μL of diluted Nafion solution (water : 5 wt% Nafion = 4 : 1) was layered on the surface of the modified electrode and allowed to dry. The preparation of RuO_2 and Pt/C is the same as the above prepared samples, where the

loading of Ru and Pt is 532.5 and 141.6 µg cm^{-2}, respectively. The RHE calibration was in the high purity hydrogen saturated electrolyte with a Pt wire as the working electrode. The average of the two potentials at which the current crossed zero was taken to be the thermodynamic potential for the hydrogen electrode reactions. The LSV with iR correction was used to evaluate the OER performance under room temperature at a scan rate of 5 mV s^{-1}. For the measurement with iR-correction, R was referred to as the ohmic resistance arising from the electrolyte/contact resistance of the setup. The 100% iR-correction was performed manually after the measurement (Figure S51). The measured current density (j) was obtained by the equation: j = current (I) / disk area (S). By plotting overpotential η against log $|j|$ from LSV curves, Tafel slopes can be gained. The exchange current density was calculated from the cross points between Tafel curves and the x-axis (at overpotential of 0 V). The electrochemical surface areas (ECSA) were evaluated by CV curves at the potential window of 0.7 to 0.8 V vs. RHE with different scan rates of 20, 40, 60, 80, 100 mV s^{-1}, respectively. By plotting the Δj/2$_{0.75 \text{ vs. RHE}}$-scan rate curves, the linear slopes were used to represent the ECSA values. The lower limit TOF was calculated by approximating that all metal centers contribute to the OER. Specifically, the lower limit TOF was calculated by the following equation: TOF = j / nN$_s$F, where j is the current density measured at a certain potential, n is the electron transfer number of the OER (n = 4), N$_s$ is the total metal amount in the catalyst deposit at the surface of the electrode, and F is Faraday constant. The total catalyst loading for the Ru SAs-CoO$_x$ electrode is 708 µg cm^{-2} (50 µg/0.0706 cm^2 = 708 µg cm^{-2}). The Ru content in Ru SAs-CoO$_x$ is 5.16 wt%, thus Ru loading for the Ru SAs-CoO$_x$ electrode is 36.5 µg cm^{-2} (0.0516 * 708 µg cm^{-2} = 36.5 µg cm^{-2}) and CoO$_x$ loading for the Ru SAs-CoO$_x$ electrode is = 708 - 36.5 = 671.5 µg cm^{-2}. Then, the stoichiometry of CoO$_x$ can be approximated as Co$_3$O$_4$. By taking into account the molar mass of Ru (M(Ru) = 101.07 g mol^{-1}) and Co$_3$O$_4$ (M(Co$_3$O$_4$) = 240.8 g mol^{-1}), the value of N$_s$(Ru) and N$_s$ (Co) could be obtained. N$_s$(Ru) = 36.5 * 10^{-6} g cm^{-2}/101.07 g mol^{-1} = 3.61 * 10^{-7} mol cm^{-2}; N$_s$ (Co) = 3 * N$_s$ (Co$_3$O$_4$) = 3 * 671.5 * 10^{-6}/240.8 = 8.37 * 10^{-6} mol cm^{-2}. Therefore, the total amount of metal cations at the Ru SAs-CoO$_x$ electrode is Ns = N$_s$(Ru) + N$_s$(Co) = 8.73 * 10^{-6} mol cm^{-2}. For the RuO$_2$ electrode, the Ru loading for the RuO$_2$ electrode is = 532.5 µg cm^{-2}, which gives N$_s$(Ru) = N$_s$ = 532.5 * 10^{-6}/101.07 = 5.27 * 10^{-6} mol cm^{-2}. For the Co$_3$O$_4$ electrode, the Co loading for the Co$_3$O$_4$ electrode is = 708 µg cm^{-2}, which gives N$_s$(Co) = N$_s$ = 3 * 708 * 10^{-6}/240.8 = 8.82 * 10^{-6} mol cm^{-2}. The OER faraday efficiency experiment was conducted using the water drainage method, with a current density of 20 mA cm^{-2}. Each experiment lasted for ten minutes and was repeated six times. The geometric surface area measured 1 cm^2, while the catalyst loading was 0.3 mg cm^{-2}. To prepare working electrode for durability tests, 5 mg of the as-prepared catalyst, 100 µL of 5 wt% Nafion, 100 µL of ethanol, and 800 µL of DI water were ultrasonically dispersed into a uniform solution. Then 100 µL of the catalyst ink was deposited on the carbon cloth (1×1 cm^2) and allowed to dry. Durability was evaluated using catalysts loaded carbon cloth (1 cm^2) with mass loadings of 0.3 mg cm^{-2}. The samples after the durability test were used for characterization while supported on carbon cloth. The acidic electrolyzer tests were carried out in a standard two-electrode system. The electrode preparation procedure for the acidic electrolyzer tests was identical to that of OER tests. The catalyst dissolution rate was evaluated using catalysts loaded carbon cloth (1 cm^2) with mass loadings of 0.3 mg cm^{-2}. The catalyst dissolution rate during chronopotentiometry tests were performed at 10 mA cm^{-2} in 25mL of 0.1 M HClO$_4$ solution. Thus, the amount of Co and Ru dissolution can be obtained by monitoring the concentration of Ru and Co in the electrolyte by ICP-MS.

In situ DEMS experiment

In situ DEMS experiment was performed on an in situ differential electrochemical mass spectrometer provided by Linglu Instruments (Shanghai) Co. Ltd. A typical test was carried out in a three-electrode cell with N$_2$ saturated 0.1 M HClO$_4$ as electrolyte. Firstly, the samples were labelled with ^{18}O isotopes in ^{18}O-labelled 0.1 M HClO$_4$ at 1.7 V (vs. RHE) for 10 min. Due to the involvement of lattice oxygen exchange with water during the LOM process, the ^{18}O can be incorporated into the material after OER reaction is carried out in ^{18}O-labelled 0.1 M HClO$_4$ for a period of time. Then the electrodes were rinsed with ^{16}O water to remove H$_2$^{18}O. In addition, CV tests were performed in the range of 0.5 - 1.0 V to further purge the adsorbed ^{18}O species (such as ^{18}OH*, H$_2$^{18}O*) on the surface of samples. Finally, in situ DEMS experiment was carried out with applied potential in the range of 1.1 - 1.7 V (vs. RHE) to detect the signals of ^{34}O$_2$(^{18}O^{16}O), and ^{36}O$_2$(^{18}O^{18}O).

In situ Raman spectroscopy experiment

The in situ Raman spectra were performed on the Renishaw inVia Raman Spectrometer (laser wavelength = 532 nm). Before data collection, calibration was performed using a silicon wafer standard (520 cm^{-1}). The Raman spectra of Ru SAs-CoO$_x$ were recorded from 0 to 60 min at 1.5 V vs. RHE.

DFT calculation

The present first principle DFT calculations are performed by Vienna Ab initio Simulation Package (VASP) with the projector augmented wave (PAW) method.[1, 2] The exchange-functional is treated using the generalized gradient approximation (GGA) of Perdew-Burke-Emzerhof (PBE) functional.[3] The energy cutoff for the plane wave basis expansion was set to 450 eV and the force on each atom less than 0.03 eV Å^{-1} was set for convergence criterion of geometry relaxation. Grimme's DFT-D3 methodology was used to describe the dispersion interactions.[4] Partial occupancies of the Kohn-Sham orbitals were allowed using the Gaussian smearing method and a width of 0.05 eV. The Brillourin zone was sampled with Monkhorst mesh 2 × 2 × 1 through the computational process. The self-consistent calculations apply a convergence energy threshold of 10^{-5} eV. A 15 Å vacuum space along the z direction was added to avoid the interaction between the two neighboring images. To better account for the strong correlated interactions in transition metals, we applied U value corrections of 3.42 eV and 2.42 eV to the Co and Ru elements, respectively. Additionally, the

calculations considered the spin polarization effects. According to experimental information, we constructed a (311) surface of the Co$_3$O$_4$ structure as the reactive surface. In this structure, there are 72 Co atoms and 96 O atoms. When building the model of Ru single atom supported on the Co$_3$O$_4$ structure, we incorporated synchrotron radiation information and replaced the Co^{2+} atoms with Ru single atoms. During the structure optimization process, we considered a total of 9 atomic layers. We maintained the bottom 6 layers of atoms fixed to simulate bulk properties, while allowing the remaining atoms to optimize and simulate surface properties. $E_{f (Co)} = E_{vacancy(Co)} + E_{Co} - E_{total}$ and $E_{f (O)} = E_{vacancy(O)} + E_{O2*(1/2)} - E_{total}$, where $E_{vacancy(Co)}$ represents the energy with Co vacancy on the slab, $E_{vacancy(O)}$ represents the energy with O vacancy on the slab, E_{total} represents the energy without the vacancy on the slab, $E_{O2*(1/2)}$ is the energy of an O atom obtained by $1/2 O_2$ (g), E_{Co} is the energy of a Co atom obtained by dividing the energy of a Co bulk by the number of Co atoms comprising it. To illustrate the activity of AEM (adsorbate evolution mechanism) and LOM (lattice-oxygen-mediated mechanism), the free energy diagrams was estimated as follows: The Gibbs free energy change is shown in the following equation: $\Delta G = \Delta E + \Delta ZPE - T\Delta S$. ΔE, ΔZPE, and ΔS are the reaction energy, the change in zero point energy, and the change in entropy, respectively. The value of ΔE was determined by the computation of geometrical structures. The values of ΔZPE and ΔS were obtained by employing the computed vibrational frequencies and standard tables for the reactants and products in the gas phase. The entropy of the adsorbed atoms/molecules on the surface active sites of catalysts was assumed to be zero. The temperature dependence of the enthalpy was neglected in the calculations. The transition states during the reaction pathway were evaluated by using the climbing-image nudged elastic band (CINEB) method with convergence criteria of force below 0.05 eV Å^{-1}.

Note S1: In conventional alkaline water electrolyzer, the two electrodes are separated by a diaphragm. This diaphragm exhibits limited effectiveness in preventing the cross-diffusion of product gases, which can lead to an increase in hydrogen concentration beyond the lower explosion limit (>4 mol% H$_2$). In contrast, the polymer electrolyte membrane (PEM) displays a low gas crossover rate and possesses a compact system design with robust structural properties. Consequently, PEM electrolyzers offer higher gas purity in practical applications compared to alkaline electrolyzers.

Note S2: Meanwhile, we made a simple estimate that the stoichiometry of CoO$_x$ is Co$_3$O$_4$. Since the weight contents of Ru and Co$_3$O$_4$ in Ru SAs-CoO$_x$ are found to be 5.16 wt% and 94.84 wt% (Supplementary Table 3), respectively, the total metal proportion of Ru in Ru SAs-CoO$_x$ sample is 0.00051 mol/g (N_s(Ru) = 0.0516 /101.07 g/mol = 0.00051 mol/g), the total metal proportion of Co^{2+} is 0.0066 mol/g (N_s(Co^{2+}) = 0.9484 /240.8 g/mol * 3 * 1.28/2.28 = 0.0066 mol/g), and the total metal proportion of Co^{3+} is 0.0052 mol/g (N_s(Co^{3+}) = 0.9484 /240.8 g/mol * 3 * 1/2.28 = 0.0052 mol/g). We assume x mol/g Ru species are substituted for the Co^{2+} sites in Co$_3$O$_4$, and (0.00051-x) mol/g Ru species are substituted for the Co^{3+} sites in Co$_3$O$_4$, thus the ratio of Co^{2+}/Co^{3+} is (0.0066-x)/(0.00469+x). Therefore, according to the ratio of Co^{2+}/Co^{3+} (1.22) for Ru SAs-CoO$_x$, our estimation reveals that ~78% Ru occupies T$_d$ sites, while the remaining ~22% occupies O$_h$ sites.
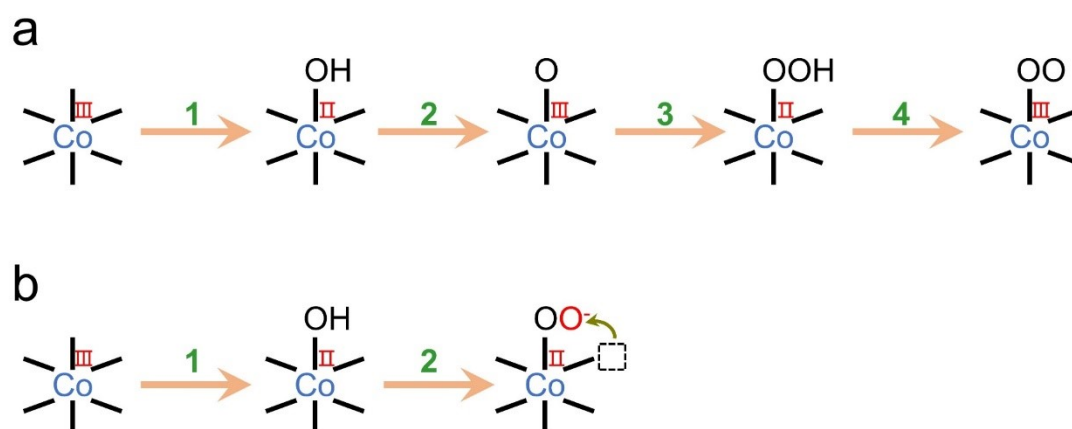

Figure S1. Recognized mechanism[5, 6] associated for the formation of O-O intermediate on the Co$_3$O$_4$ catalyst in acidic media during the (a) AEM process and (b) LOM process.
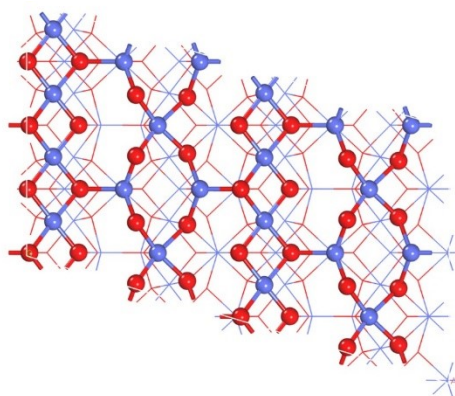
Figure S2. Slab models of the pristine Co_3O_4 structure. Blue and red balls represent Co and O atoms, respectively.

a

Ru replaced Co^{2+} (T_d) site

1.194 eV

b

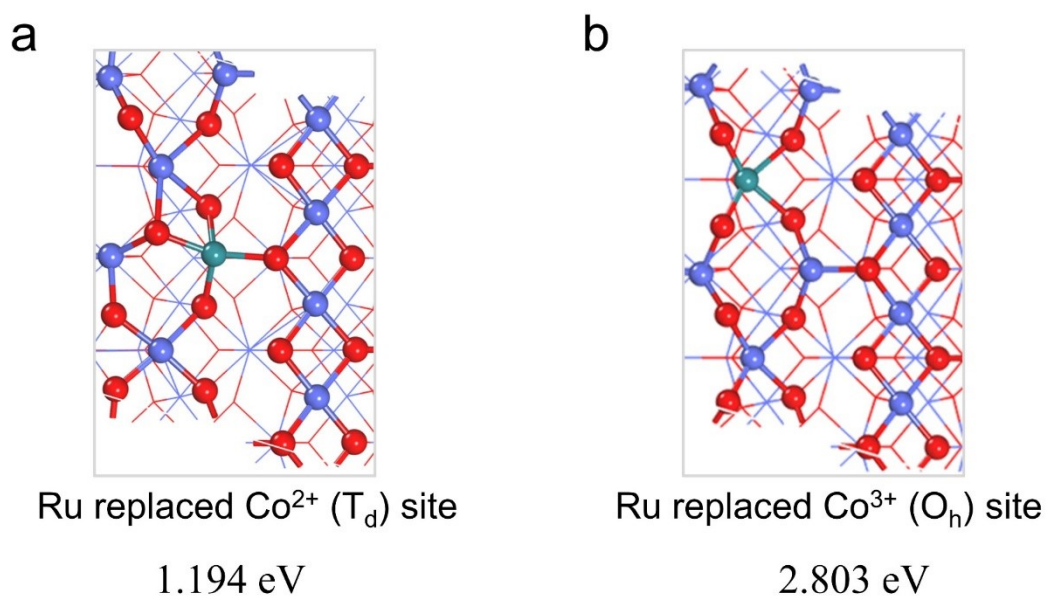Ru replaced Co^{3+} (O_h) site

2.803 eV

Figure S3. Slab models obtained by the substituting different sites on the Co_3O_4 structure for Ru atom and corresponding formation energy: (a) replacing the tetrahedral Co^{2+} (T_d) site with Ru, (b) replacing the octahedral Co^{3+} (O_h) site with Ru. Blue, red, and dark cyan balls represent Co, O, and Ru atoms, respectively.

Because the electrocatalytic reactions occur on the surface of electrocatalyst, we simplified the model in the DFT simulation, where Ru was only considered to be incorporated on the surface, which was utilized to provide side insight for design of electrocatalyst and lateral understanding of the structural and catalytic mechanism changes after the incorporation of Ru. In addition, after substituting the tetrahedral Co^{2+} (T_d) with Ru, a significant reduction in the distance between Ru and adjacent oxygen atoms was observed, leading to a contraction in the Ru-Co/Ru bond length and alterations to the surface structure.
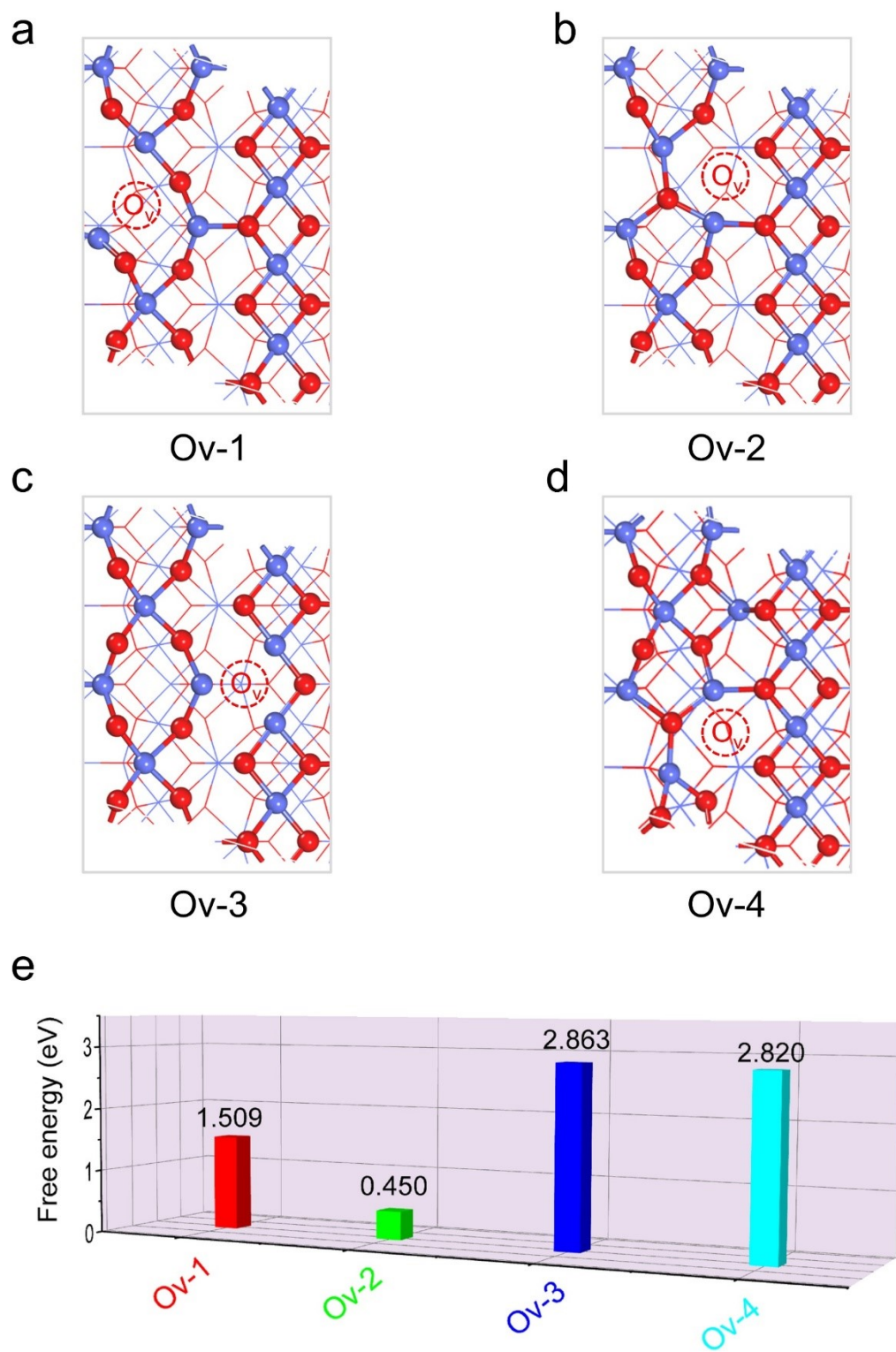
Figure S4. (a-d) Slab models of Co_3O_4 structures with varying sites of oxygen vacancy and (e) corresponding oxygen vacancy formation energies.
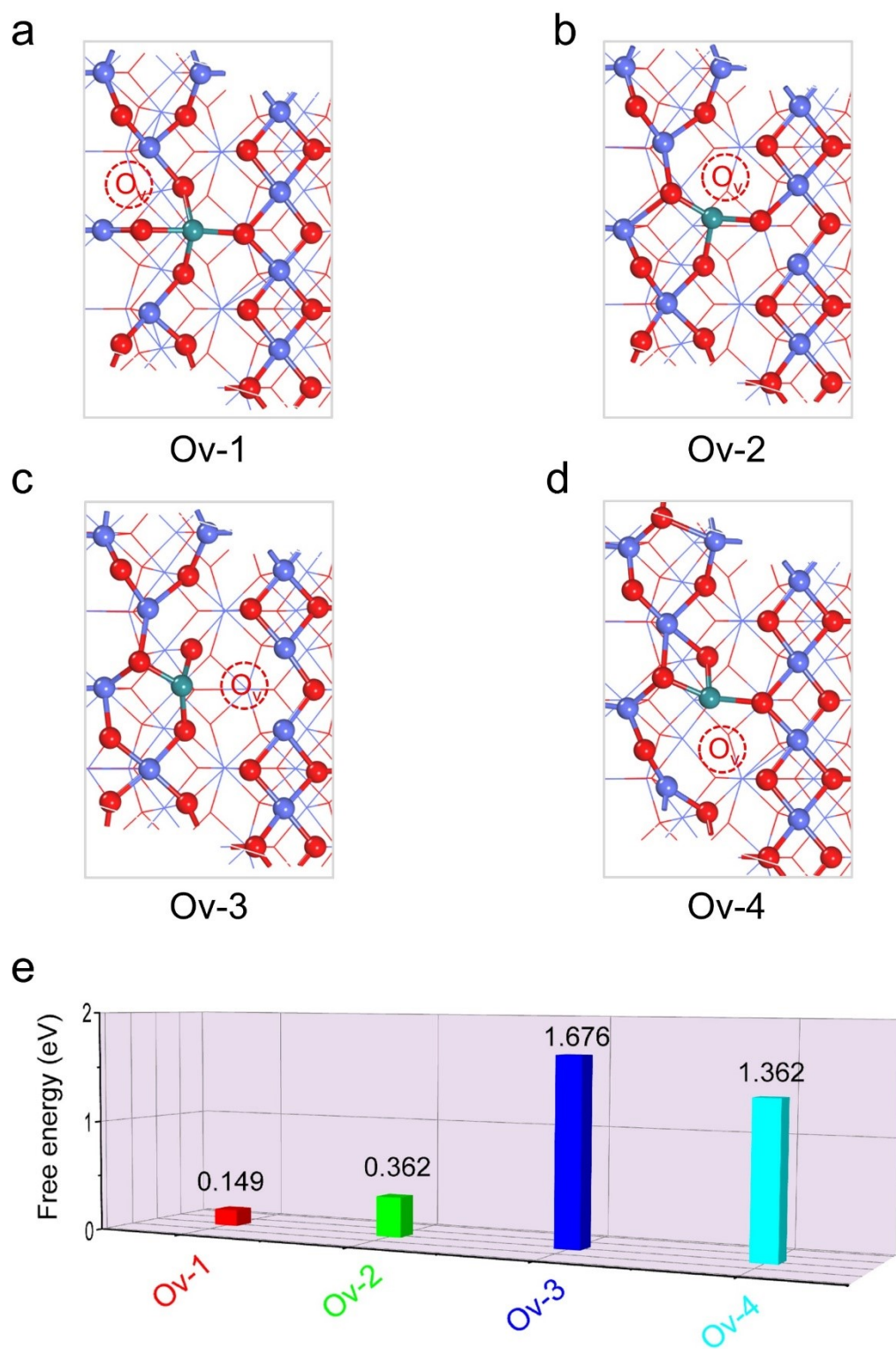
Figure S5. (a-d) Slab models of Ru-Co_3O_4 structures with varying sites of oxygen vacancy and (e) corresponding oxygen vacancy formation energies.
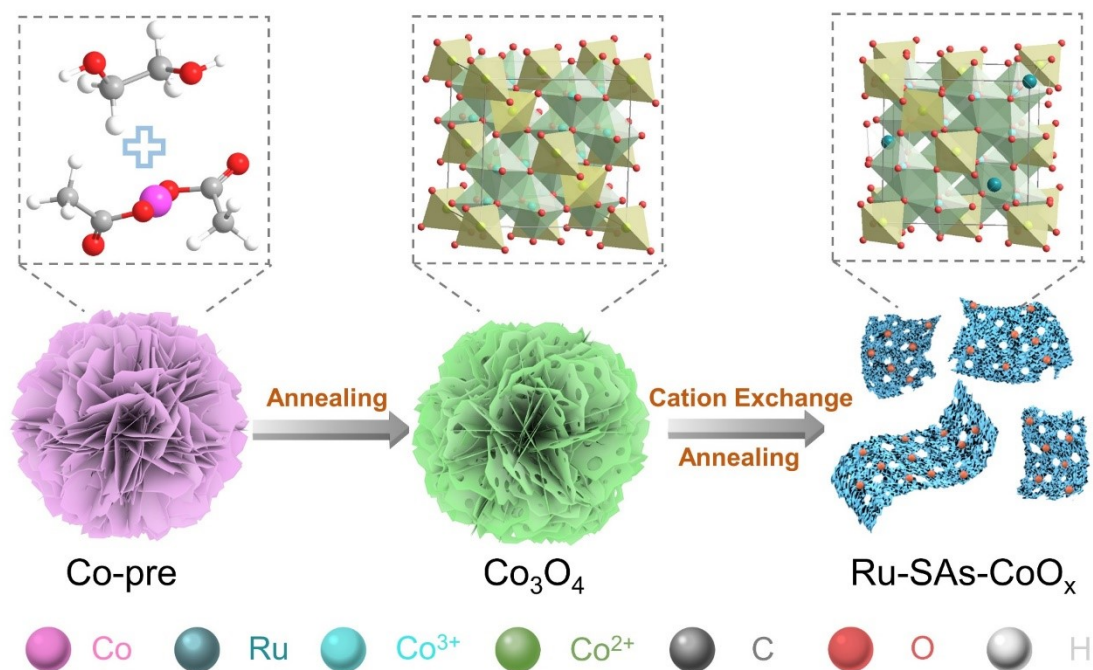
Figure S6. Synthesis scheme of Ru SAs-CoO$_x$.
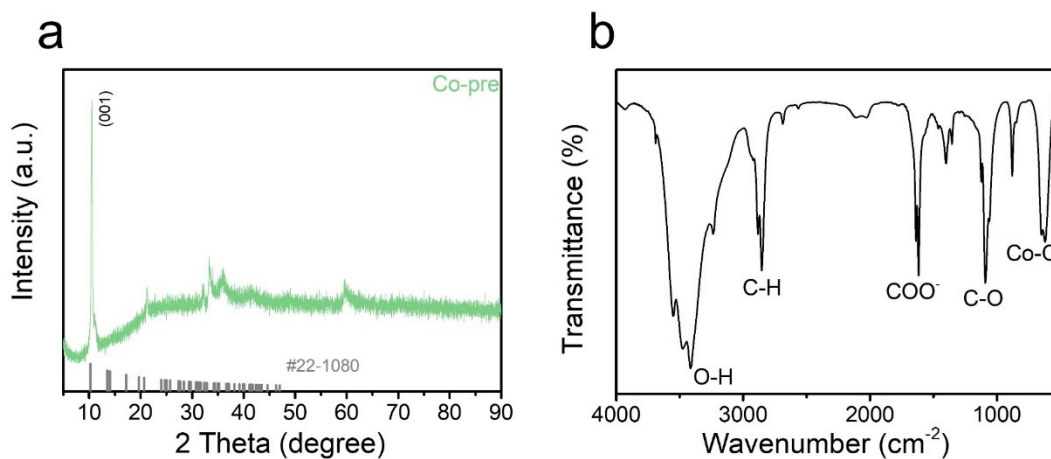
Figure S7. (a) XRD pattern of cobalt precursor (Co-pre), (b) Fourier transform infrared spectroscopy (FT-IR) spectrum of Co-pre.

As shown in the Figure S7a, the XRD pattern displayed a strong peak around 10°. Although it lacks a specific crystal structure, its crystal arrangement closely resembles that of cobalt acetate hydrate [#22-1080]. This peak is likely attributed to the coordination and alcoholysis of EG with Co(CH$_3$COO)$_2$.[7] Fourier transform infrared spectroscopy (FT-IR) analysis revealed that the C-H stretching vibrations at 2854 cm^{-1} correspond to C-H bonds of ethanediol, while the absorptions bands at 1610 cm^{-1} could be attributed to the acetates linked to cobalt cations (Figure S7b).[8] Therefore, the chemical composition of the Co-pre involves. a cobalt alkoxide linked to acetates.
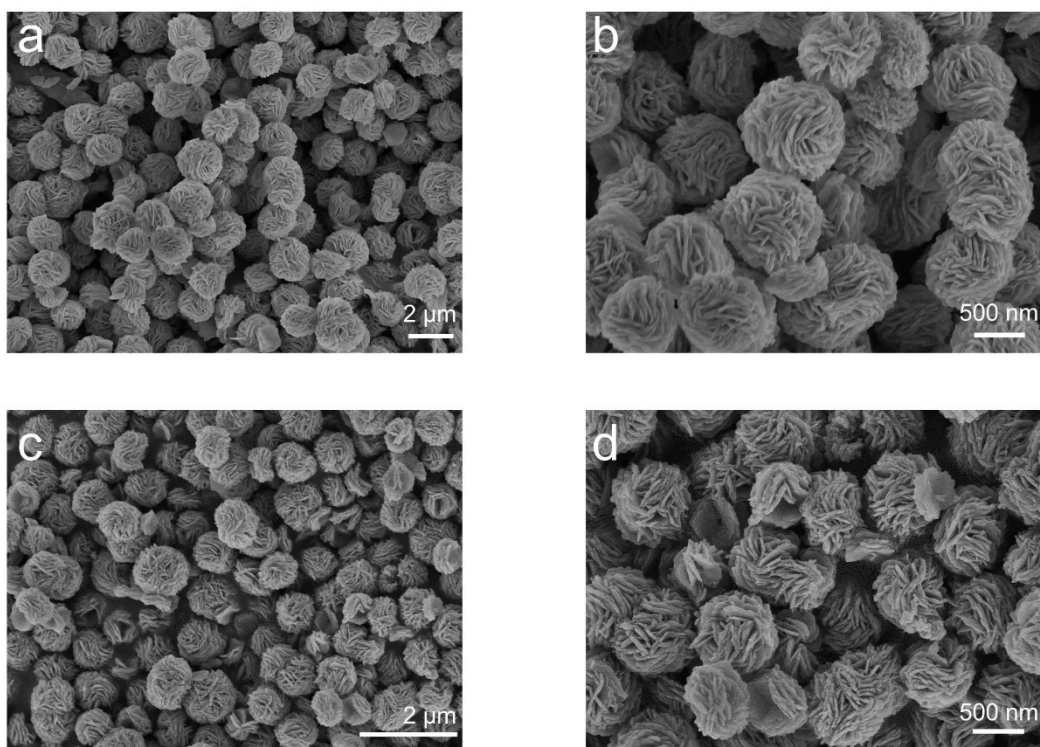
Figure S8. SEM images of (a-b) cobalt precursor (Co-pre) and (c-d) pristine Co_3O_4 with "flower-like" morphology.

The flower-like morphology maintained well after the first calcination treatment, indicating that morphology was not affected by the calcination treatment. In addition, the condition of the second calcination treatment was similar to the first calcination treatment. Therefore, calcination has little effect on the morphology. Thus, we believe that the changes of morphology are attributed to the "etching recombination" that occurred during the cation exchange process (the substitution of Ru for Co).
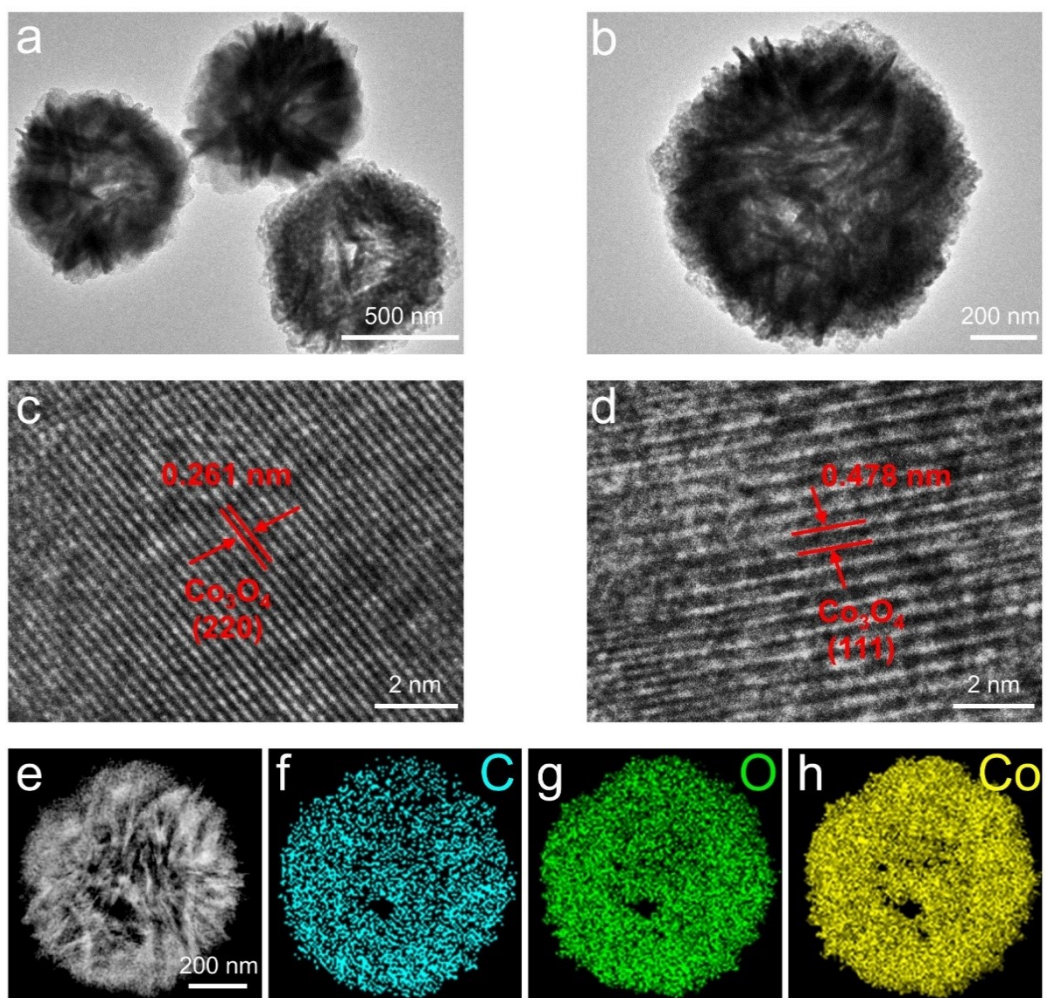
Figure S9. (a, b) TEM and (c, d) HRTEM images of pristine Co_3O_4; (e-h) HAADF-STEM images of the Co_3O_4 and corresponding elemental mapping images of C, O and Co.
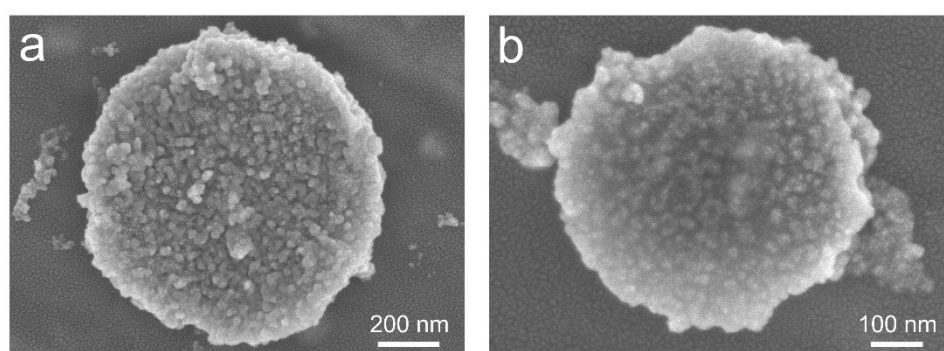
Figure S10. (a, b) SEM images of the Ru SAs-CoO$_x$.
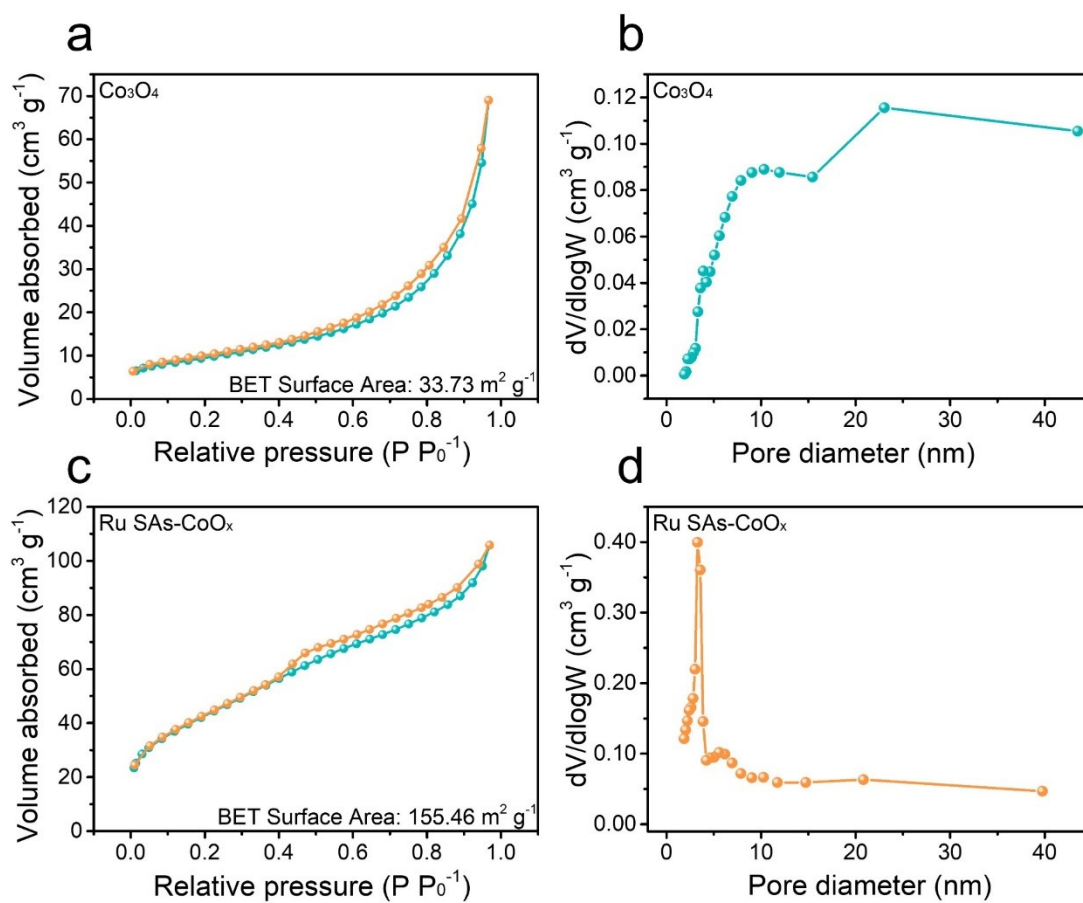
Figure S11. N_2 adsorption-desorption isotherms and pore size distribution of (a-b) Co_3O_4 and (c-d) Ru SAs-CoO$_x$.
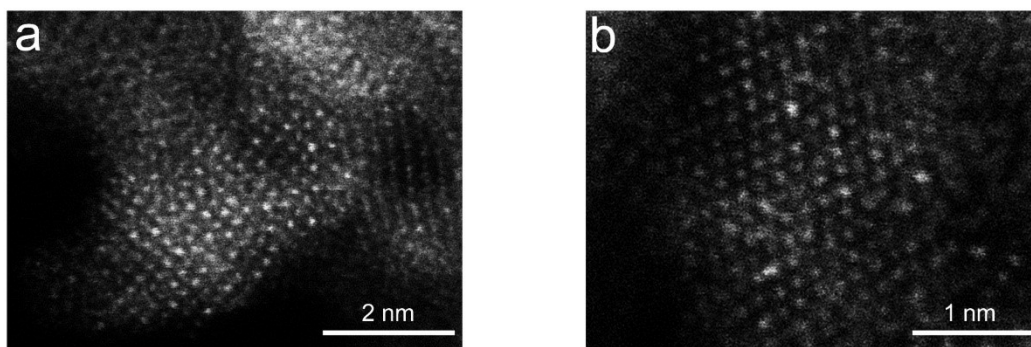
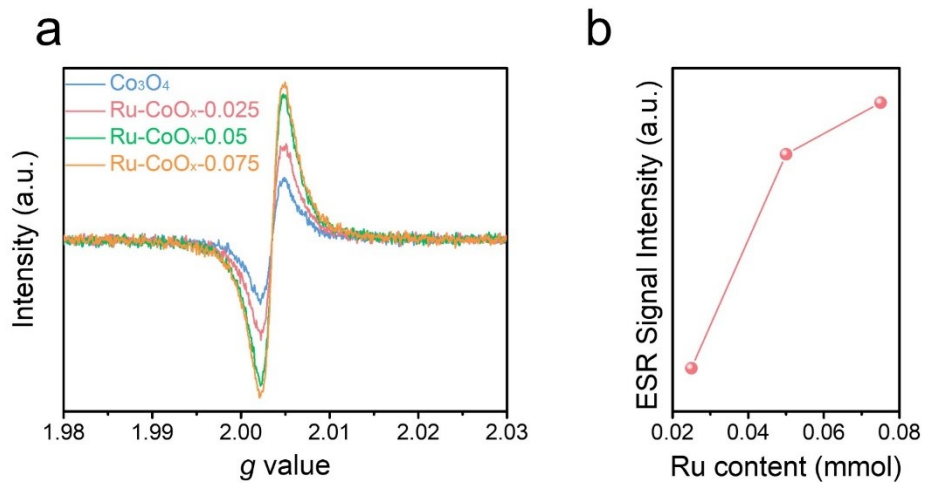**Figure S12.** HAADF-STEM images of Ru SAs-CoO$_x$ within different regions. The atomic isolation of Ru can be observed.

Figure S13. (a) ESR spectra of Co_3O_4 and Ru-CoO_x with different Ru content. (b) Intensity relationship between Ru content and ESR signal intensity.
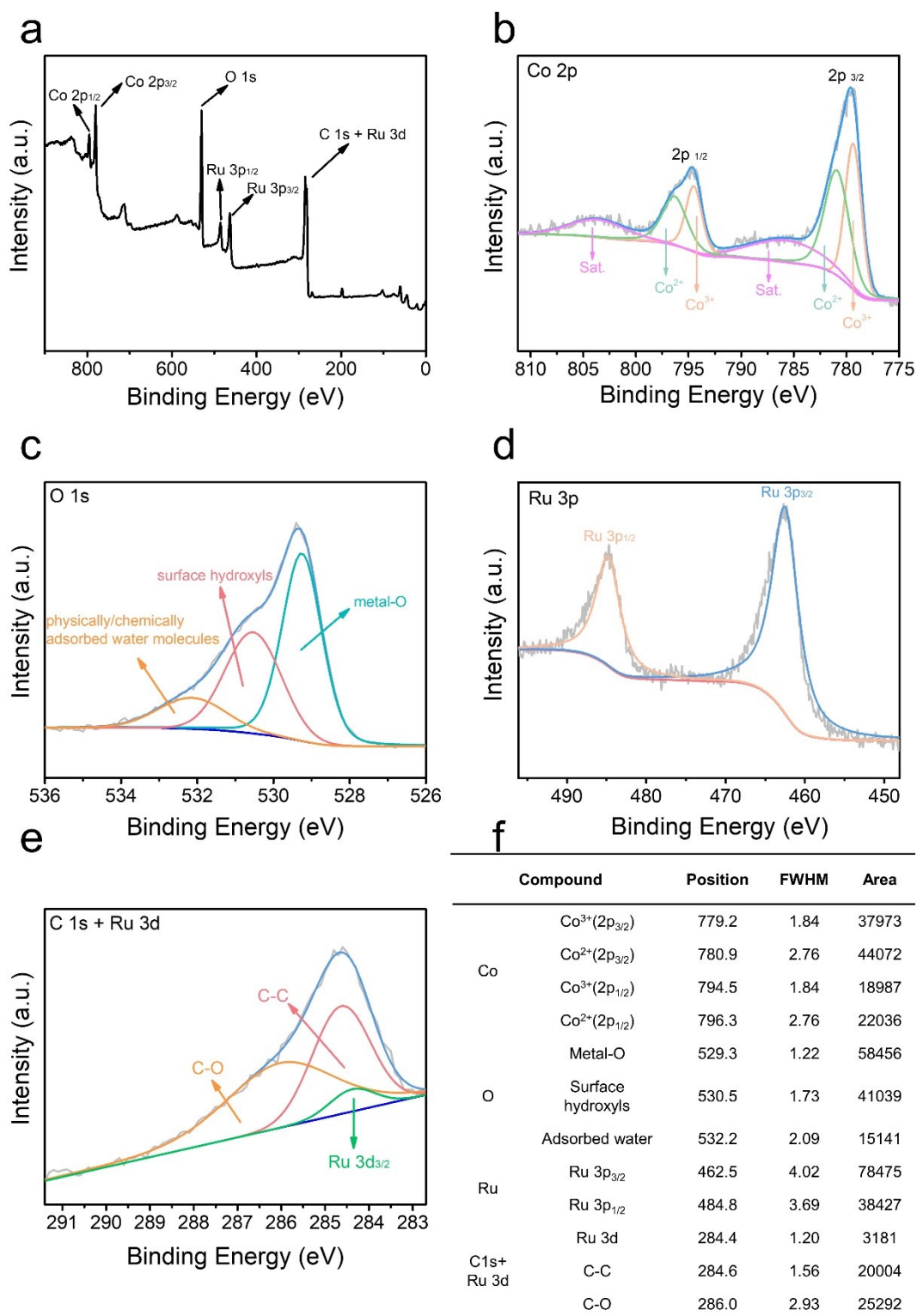
Figure S14. XPS spectra of the Ru SAs-CoO$_x$ (a) survey, (b) Co 2p, (c) O 1s, (d) Ru 3p, (e) C 1s + Ru 3d, (f) XPS fitting parameters.
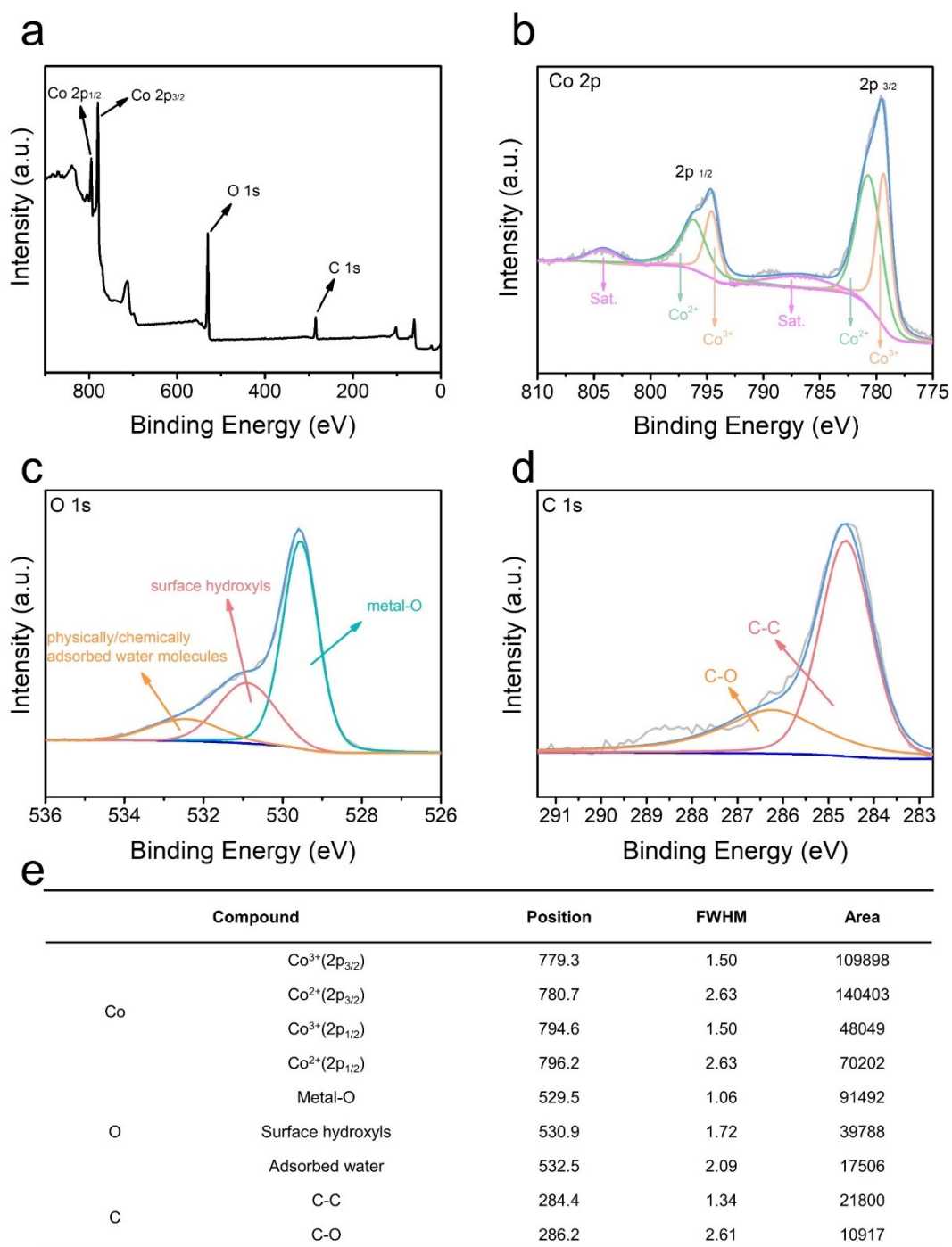
Figure S15. XPS spectra of the pristine Co_3O_4 (a) survey, (b) Co 2p, (c) O 1s, (d) C 1s, (e) XPS fitting parameters.

	Compound	Position	FWHM	Area
Co	$Co^{3+}(2p_{3/2})$	779.3	1.50	109898
	$Co^{2+}(2p_{3/2})$	780.7	2.63	140403
	$Co^{3+}(2p_{1/2})$	794.6	1.50	48049
	$Co^{2+}(2p_{1/2})$	796.2	2.63	70202
O	Metal-O	529.5	1.06	91492
	Surface hydroxyls	530.9	1.72	39788
	Adsorbed water	532.5	2.09	17506
C	C-C	284.4	1.34	21800
	C-O	286.2	2.61	10917

After the second calcination treatment, the C-O/C-C ratio of Ru SAs-CoO$_x$ (1.41) was found to be higher than that of pristine Co_3O_4 (0.50), which was attributed to an increase in oxygen content of carbon resulting from the second calcination treatment.

14

a

	Compound	Position	FWHM	Area
Ru SAs-CoO$_x$	Ru 3p$_{3/2}$	462.5	4.02	78475
	Ru 3p$_{1/2}$	484.8	3.69	38427
RuO$_2$	Ru 3p$_{3/2}$	462.5	4.22	97556
	Ru 3p$_{1/2}$	484.7	3.94	37106

b
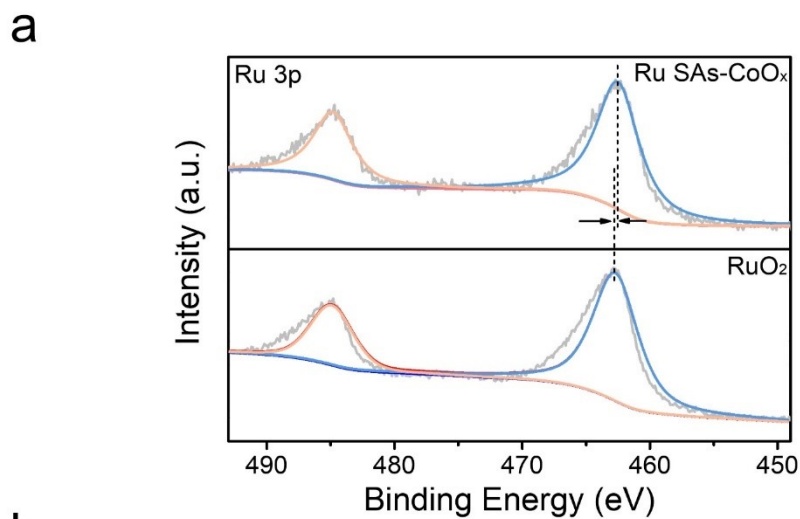
Figure S16. (a) Ru 3p XPS spectra of Ru SAs-CoO$_x$ and RuO$_2$, (b) XPS fitting parameters.

As shown in the Figure S16, the Ru 3p$_{3/2}$ binding energy of Ru SAs-CoO$_x$ is 0.3 eV lower than that of RuO$_2$, indicating a lower oxidation state of Ru in Ru SAs-CoO$_x$ compared with that in RuO$_2$.
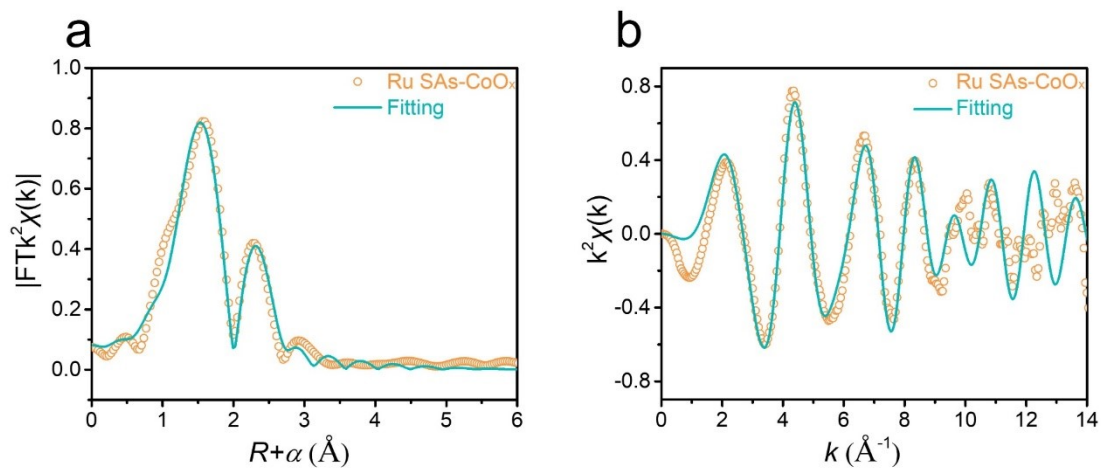
Figure S17. Ru K-edge EXAFS of Ru SAs-CoO$_x$ and the corresponding fitting curves at (a) R space and (b) K space.
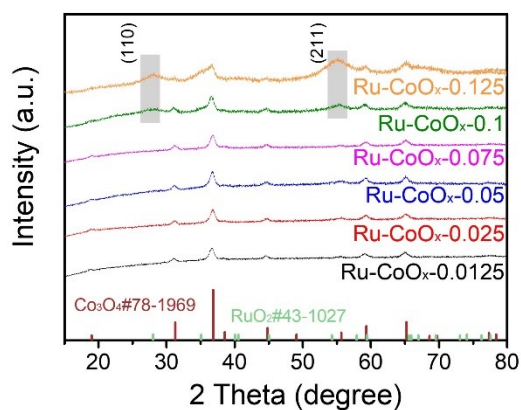
Figure S18. XRD patterns of Ru-CoOₓ with different Ru content.

As shown in the Fig.S18, no distinct second phase was detected with the increasing of Ru doping (from 0.0125 - 0.125 mmol) in this work. However, the XRD patterns of Ru-CoOₓ-0.1 and Ru-CoOₓ-0.125 exhibited a slight increase in peak width and intensity at ca. 28.0 and 54.2, which may be attributed to the (110) and (211) facets of RuO_2, indicating the formation of some poorly crystalline RuO_2 in samples with high Ru content doping.
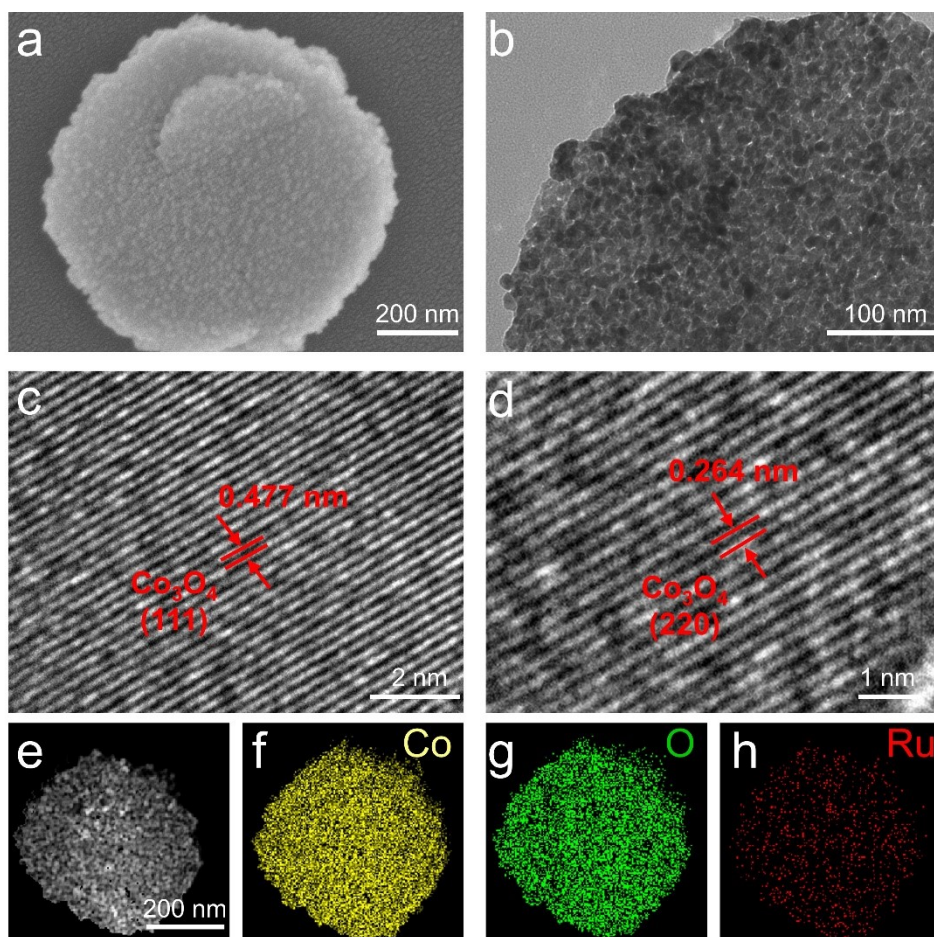

Figure S19. (a) SEM images of Ru-CoOₓ-0.0125, (b) TEM images of Ru-CoOₓ-0.0125, (c, d) HRTEM images of pristine Ru-CoOₓ-0.0125; (e-h) HAADF-STEM images of the Ru-CoOₓ-0.0125 and corresponding elemental mapping images of Co, O and Ru.
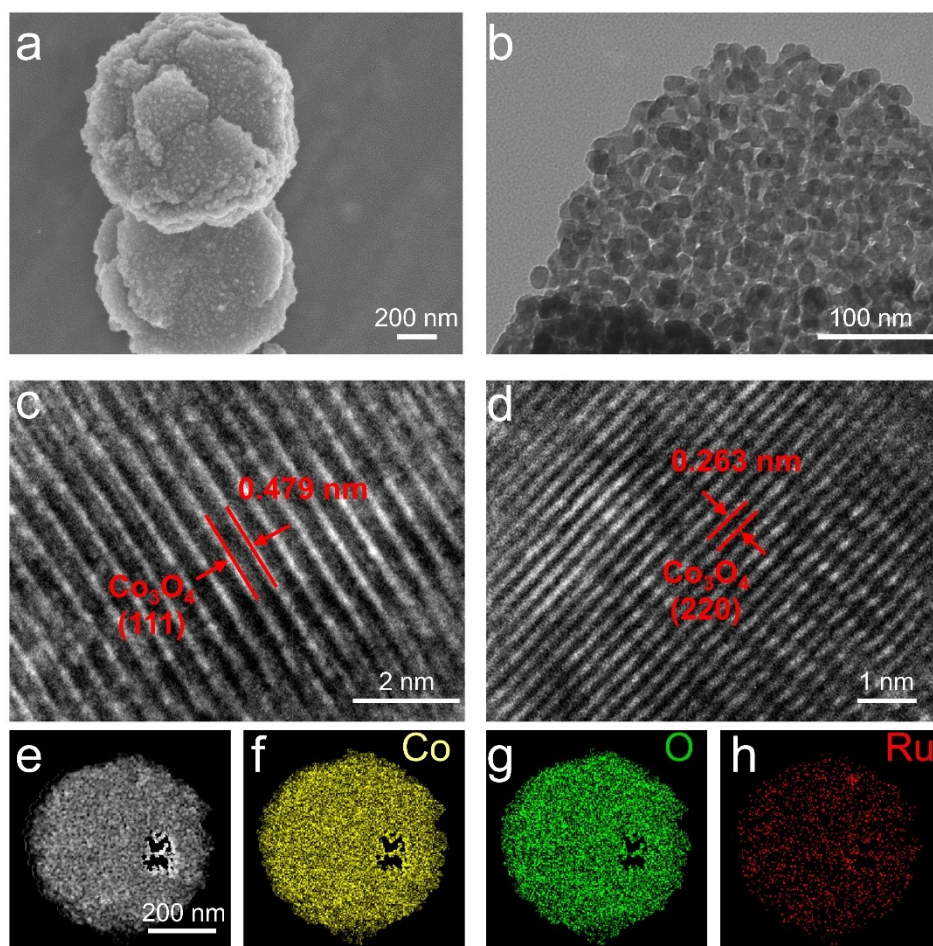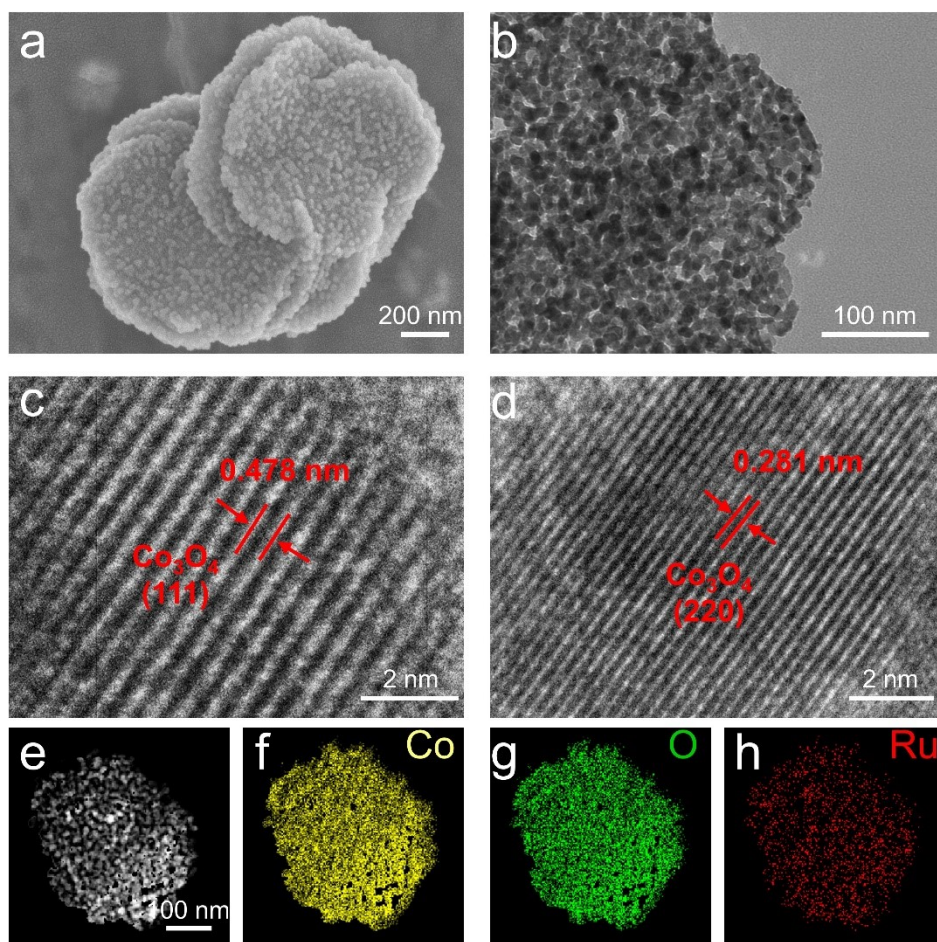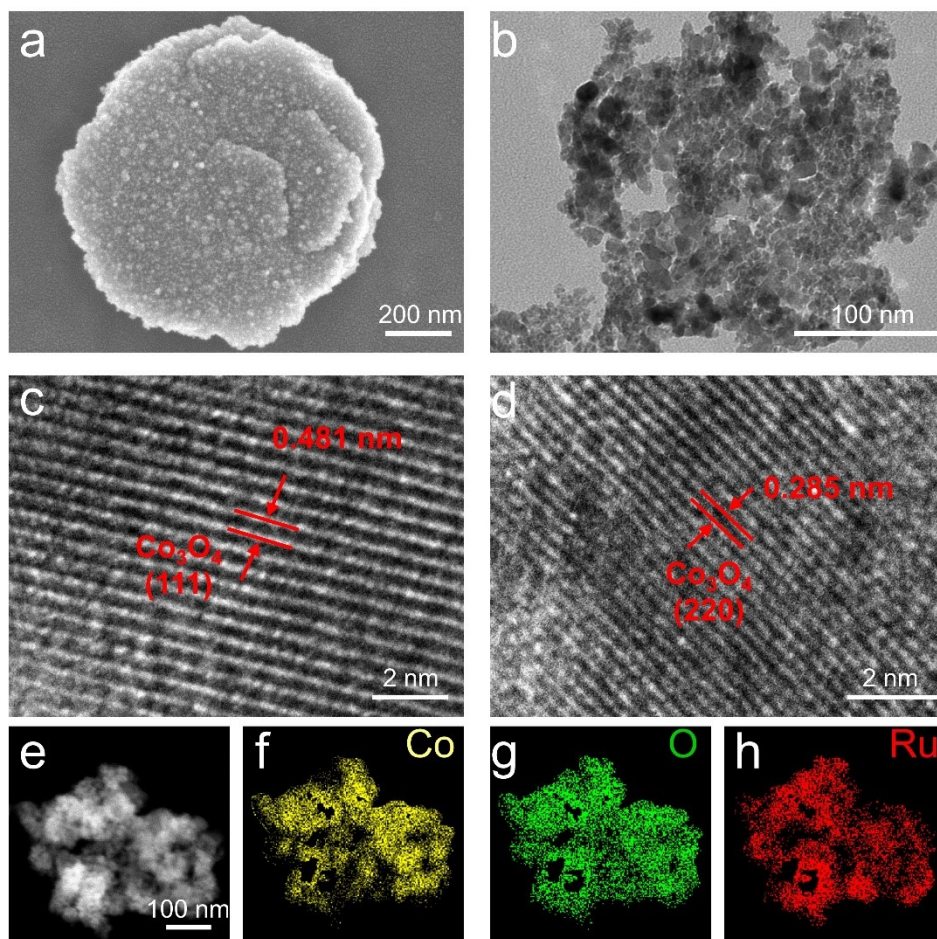
Figure S20. (a) SEM images of Ru-CoO$_x$-0.025, (b) TEM images of Ru-CoO$_x$-0.025, (c, d) HRTEM images of pristine Ru-CoO$_x$-0.025; (e-h) HAADF-STEM images of the Ru-CoO$_x$-0.025 and corresponding elemental mapping images of Co, O and Ru.
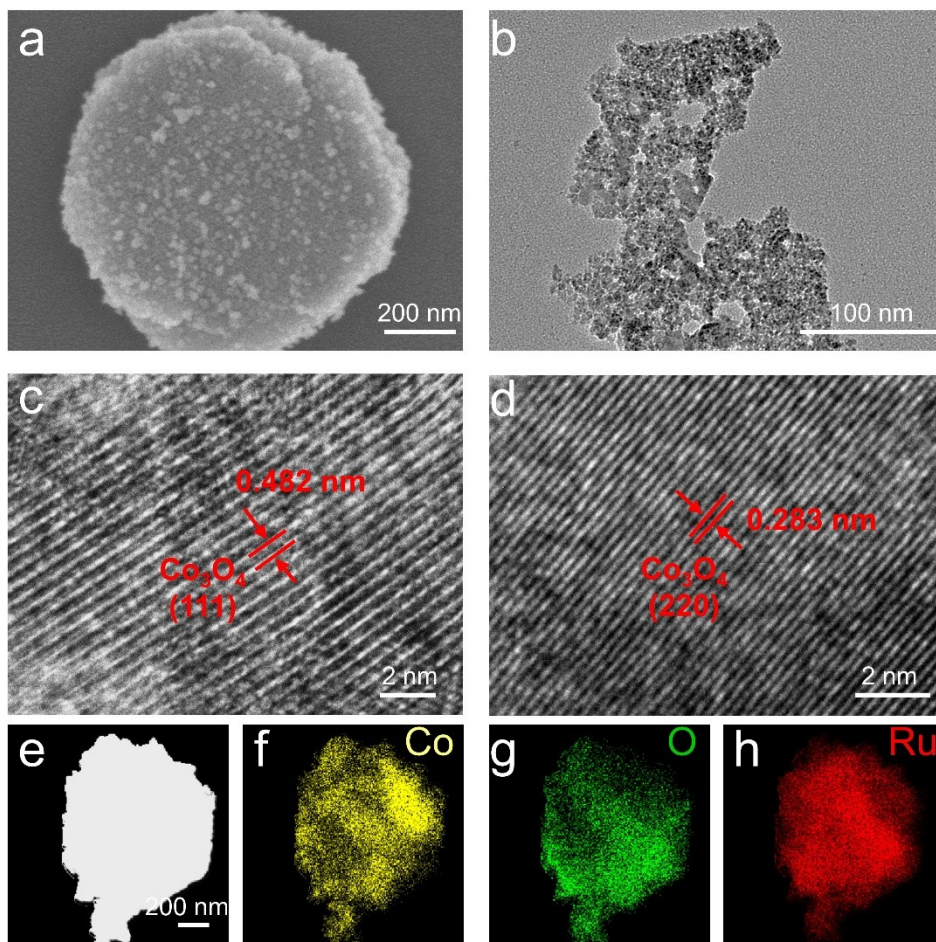
Figure S21. (a) SEM images of Ru-CoO$_x$-0.05, (b) TEM images of Ru-CoO$_x$-0.05, (c, d) HRTEM images of pristine Ru-CoO$_x$-0.05; (e-h) HAADF-STEM images of the Ru-CoO$_x$-0.05 and corresponding elemental mapping images of Co, O and Ru.

Figure S22. (a) SEM images of Ru-CoO$_x$-0.10, (b) TEM images of Ru-CoO$_x$-0.10, (c, d) HRTEM images of pristine Ru-CoO$_x$-0.10; (e-h) HAADF-STEM images of the Ru-CoO$_x$-0.10 and corresponding elemental mapping images of Co, O and Ru.
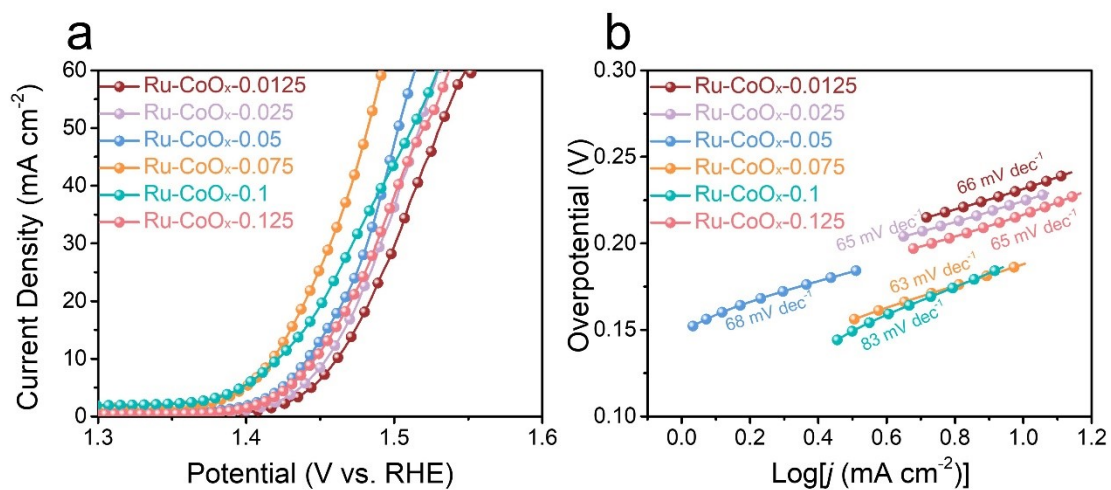
Figure S23. (a) SEM images of Ru-CoO$_x$-0.125, (b) TEM images of Ru-CoO$_x$-0.125, (c, d) HRTEM images of pristine Ru-CoO$_x$-0.125; (e-h) HAADF-STEM images of the Ru-CoO$_x$-0.125 and corresponding elemental mapping images of Co, O and Ru.

Figure S24. OER activity of Ru-CoO$_x$ with different Ru contents. (a) Polarization curves, (b) corresponding Tafel plots.

The experimental results showed that the catalytic activity did not monotonically increase with the increase of Ru content, indicating that the catalytic activity depended on both Ru and Co$_3$O$_4$. Therefore, the Ru content was at an optimum value in Ru-CoO$_x$-0.075.
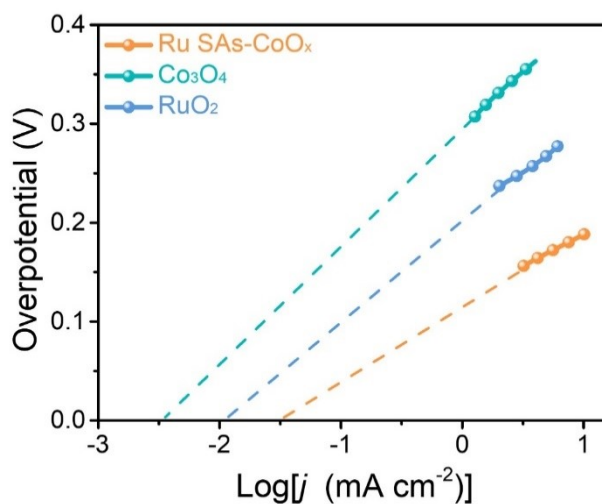

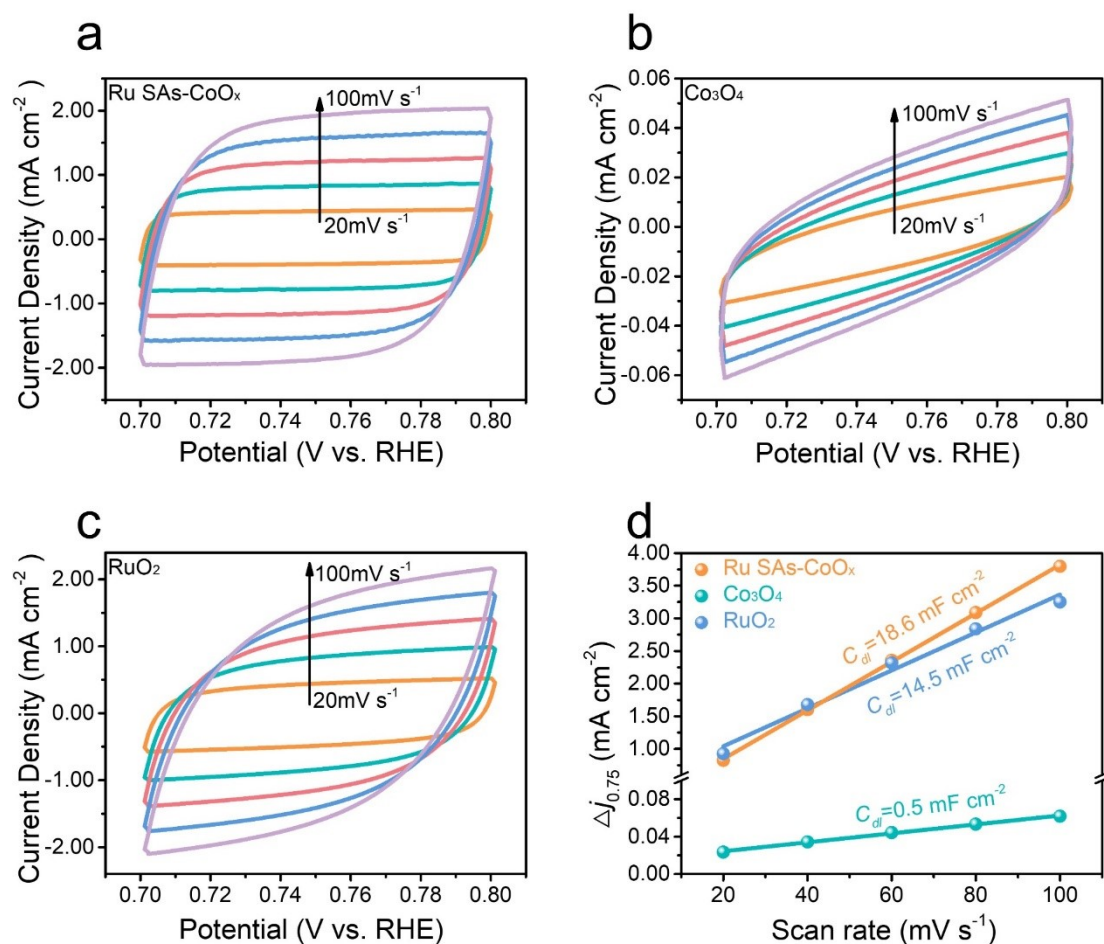**Figure S25.** The exchange current densities of the Ru SAs-CoO$_x$, Co$_3$O$_4$, and RuO$_2$.

Figure S26. CV curves at different scan rates (mV s^{-1}) for (a) Ru SAs-CoO$_x$, (b) Co$_3$O$_4$, and (c) RuO$_2$. (d) The current density differences vs scan rates and corresponding yielded C_{dl}.

As shown in Figure S26, the ECSA of Ru SAs-CoO$_x$ is much larger than that of Co$_3$O$_4$, indicating that more active area was generated after the introduction of Ru. However, considering the limited catalytic activity of original Co$_3$O$_4$ in both acidic and alkaline environments,[9-11] the enhanced intrinsic activity is mainly attributed to the low thermodynamic energy barrier (i.e., low onset potential) resulting from the introduction of Ru, despite changes in morphology influencing the ECSA.
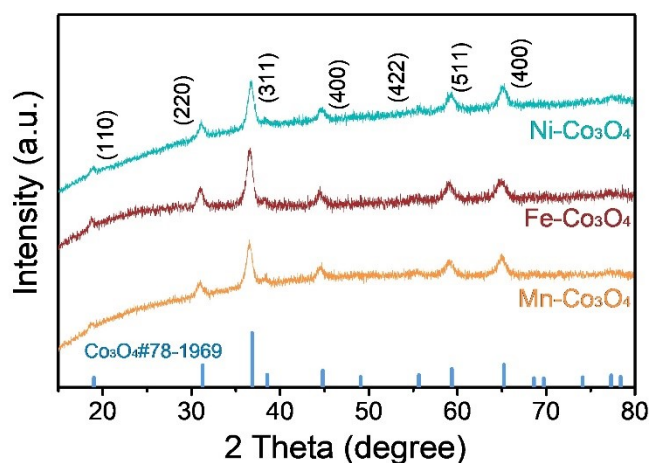

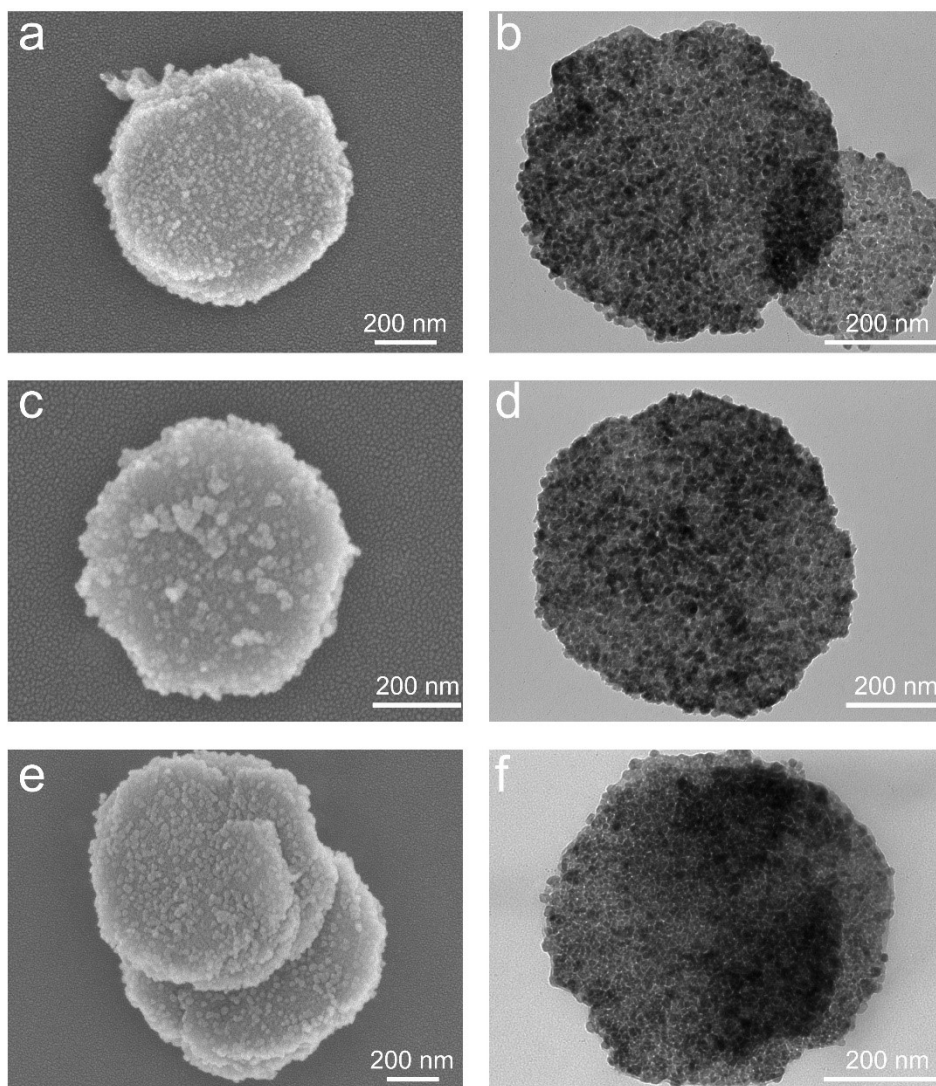**Figure S27.** XRD patterns of Mn-CoO$_x$, Fe-CoO$_x$, and Ni-CoO$_x$.

22

Figure S28. (a) SEM images of Mn-CoO$_x$, (b) TEM images of Mn-CoO$_x$, (c) SEM images of Fe-CoO$_x$, (d) TEM images of Fe-CoO$_x$, (e) SEM images of Ni-CoO$_x$, (f) TEM images of Ni-CoO$_x$.
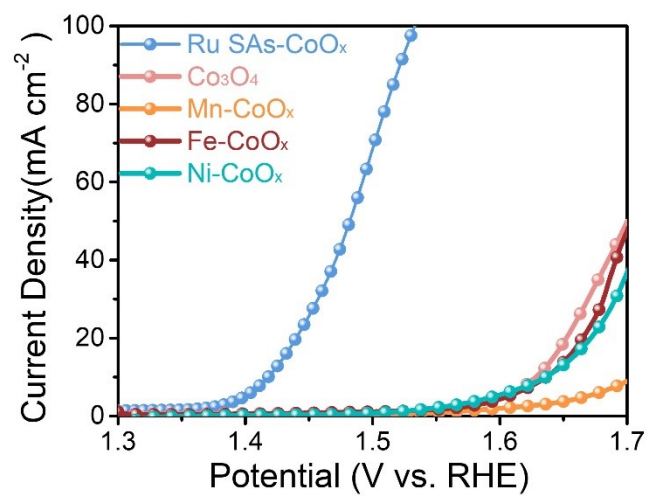

Figure S29. OER Polarization curves of Ru SAs-CoO$_x$, Co$_3$O$_4$, Mn-CoO$_x$, Fe-CoO$_x$, and Ni-CoO$_x$.
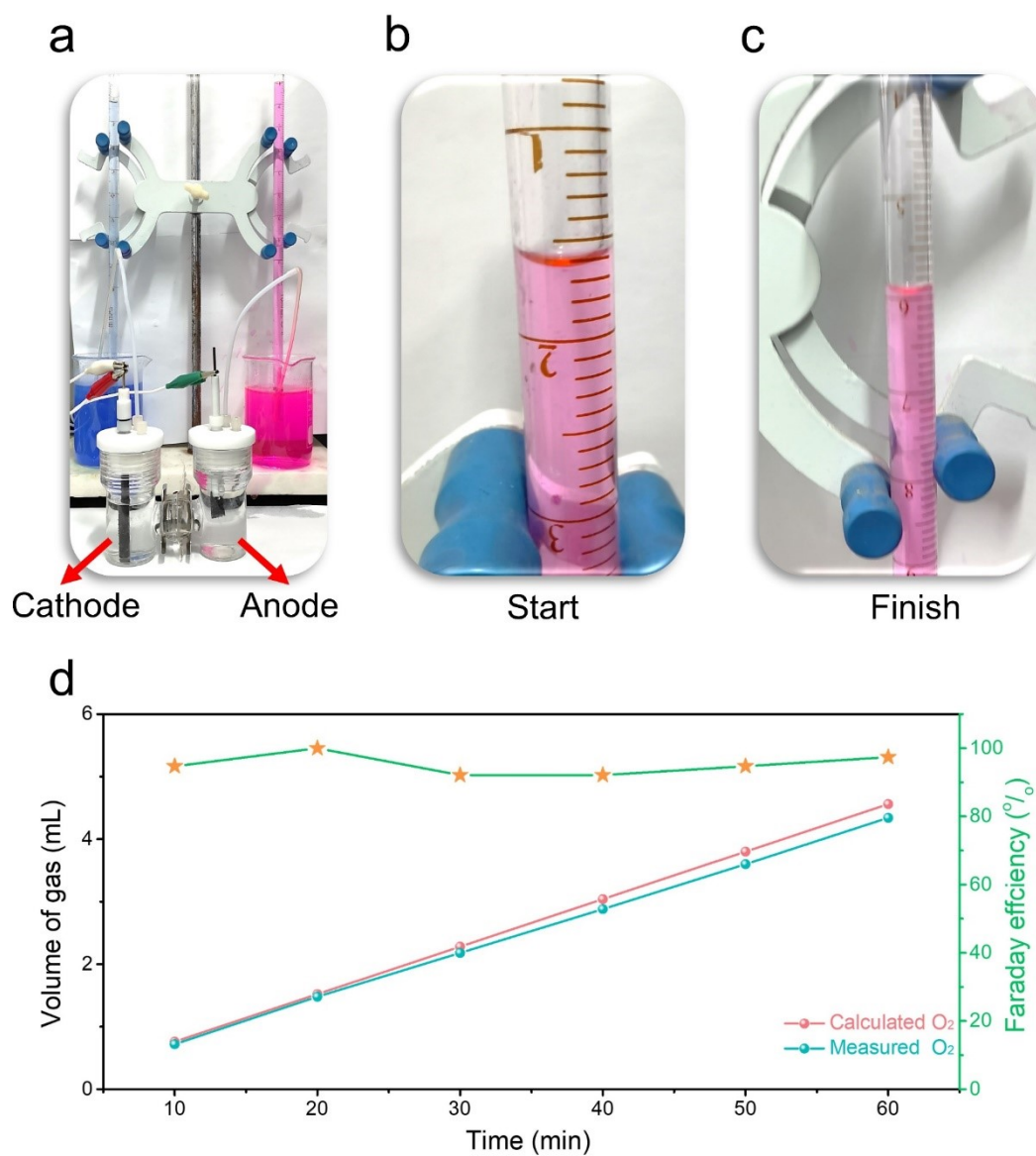
Figure S30. (a-c) Device diagram for measuring OER Faraday efficiency on Ru SAs-CoO$_x$. (d) Diagram of the amount of O$_2$ released over time in 0.1 M HClO$_4$.
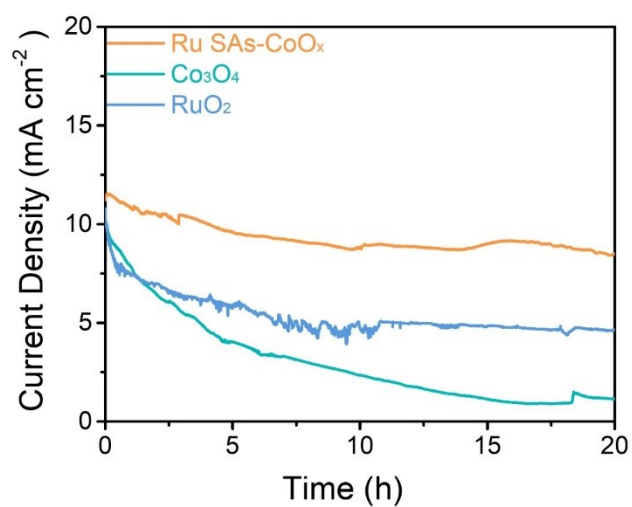

Figure S31. Potentiostatic curves of Ru SAs-CoO$_x$, Co$_3$O$_4$, and RuO$_2$ were conducted at 1.50 V, 1.83 V, and 1.58 V, respectively, where they display similar initial current density (~10 mA cm^{-2}).
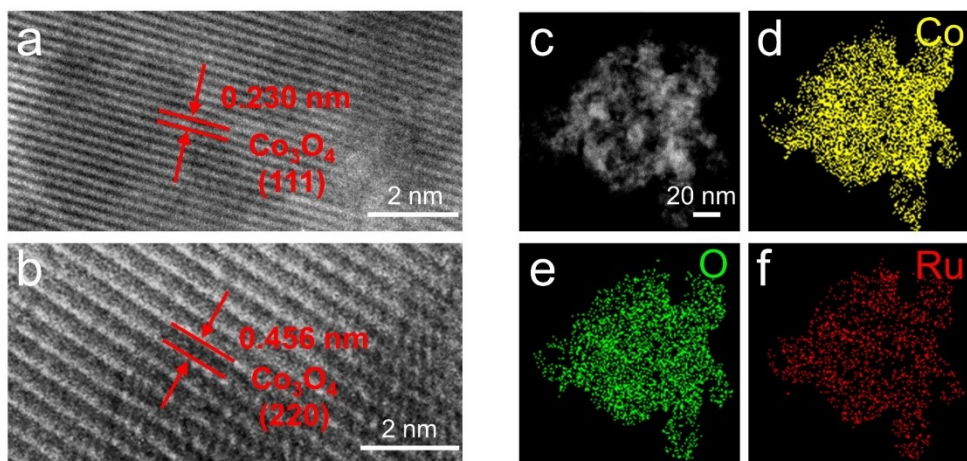
24

Figure S32. (a-b) HRTEM images of Ru SAs-CoO$_x$ after durability test. (c-f) HAADF-STEM image of the Ru SAs-CoO$_x$ and corresponding elemental mapping images of Co, O, and Ru after durability test.

However, obvious lattice shrinkage could be observed after durability test, which were attributed to the formation of amorphous cobalt oxide during the OER process.
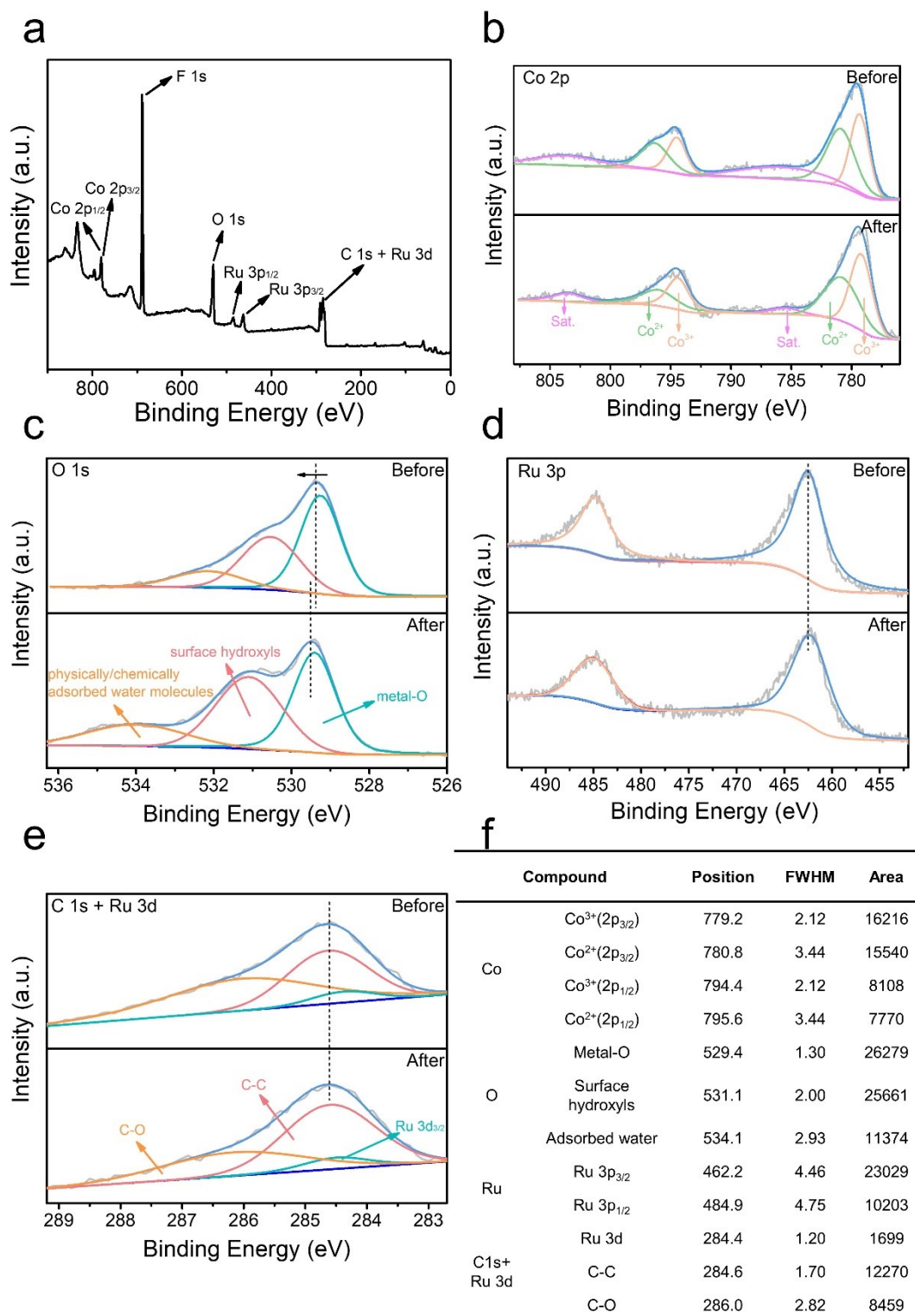
Figure S33. XPS spectra of the Ru SAs-CoO$_x$ (a) survey, (b) Co 2p, (c) O 1s, (d) Ru 3p, (e) C 1s + Ru 3d after durability test, (f) XPS fitting parameters.

Compound		Position	FWHM	Area
Co	Co^{3+}(2p$_{3/2}$)	779.2	2.12	16216
	Co^{2+}(2p$_{3/2}$)	780.8	3.44	15540
	Co^{3+}(2p$_{1/2}$)	794.4	2.12	8108
	Co^{2+}(2p$_{1/2}$)	795.6	3.44	7770
O	Metal-O	529.4	1.30	26279
	Surface hydroxyls	531.1	2.00	25661
	Adsorbed water	534.1	2.93	11374
Ru	Ru 3p$_{3/2}$	462.2	4.46	23029
	Ru 3p$_{1/2}$	484.9	4.75	10203
C1s+ Ru 3d	Ru 3d	284.4	1.20	1699
	C-C	284.6	1.70	12270
	C-O	286.0	2.82	8459

The XPS was also used to analyze the surface compositions of Ru SAs-CoO$_x$ after the durability test (Figure S33a). A slight shift was detected in Co 2p and O 1s spectra, confirming an increase in valence state under oxidative potentials. This phenomenon can be attributed the formation of cobalt oxide with a high valence state (Figure S33b-c). While no significant changes were observed in Ru 3p after durability test (Figure S33d), indicating that the incorporation of Ru atoms into the Co$_3$O$_4$ framework enhances its stability.
It should be noted that the F 1s spectra could be attributed to residual Nafion solution on the surface of catalysts.
In addition, the surface Ru content decreased from 13.68 at. % to 12.62 at. %, further demonstrating its low dissociation rate.
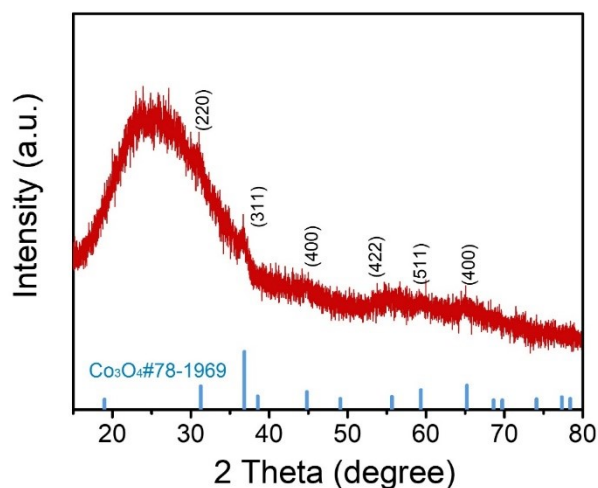
Figure S34. XRD pattern of Ru SAs-CoOₓ after durability test.

The XRD pattern exhibited the Co_3O_4 phase of Ru SAs-CoOₓ maintained well, but the peak intensity was decreased obviously, which was due to the surface composition of Ru SAs-CoOₓ partially changed into amorphous species. Due to the fact that the sample collected after the durability test was obtained from carbon cloth, the broad peak at 2θ ≈ 26° in the XRD pattern of post-OER Ru SAs-CoOₓ was attributed to a carbon signal originating from residual carbon fiber present in the carbon cloth (Figure S34).
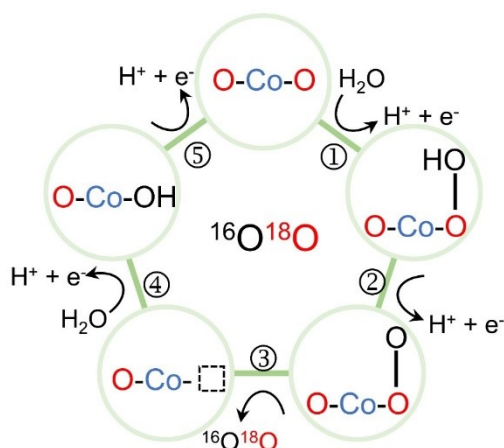

Figure S35. The illustration of LOM with the production of $^{34}O_2$.
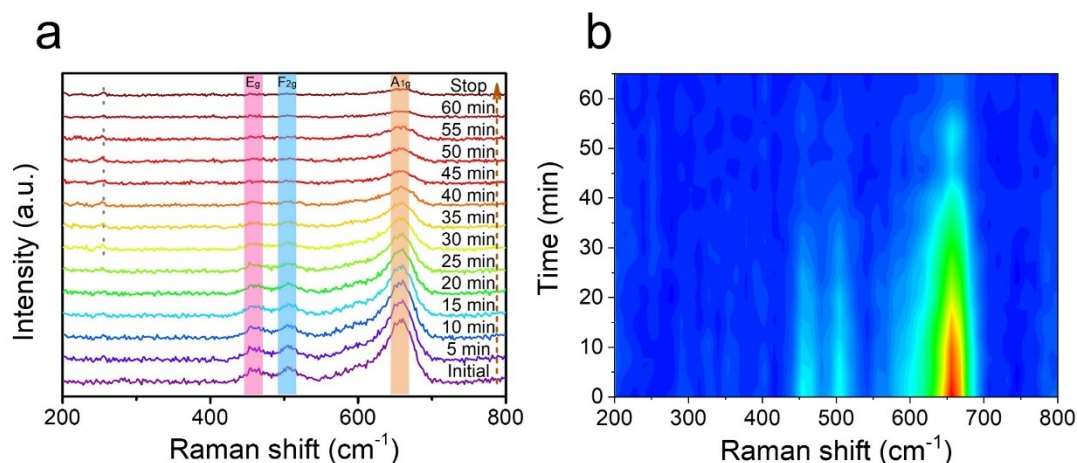

Figure S36. (a) The in-situ Raman spectra of Ru SAs-CoOₓ for OER recorded from 0 to 60 min. (b) The corresponding 2D contour diagram of in situ Raman spectra.
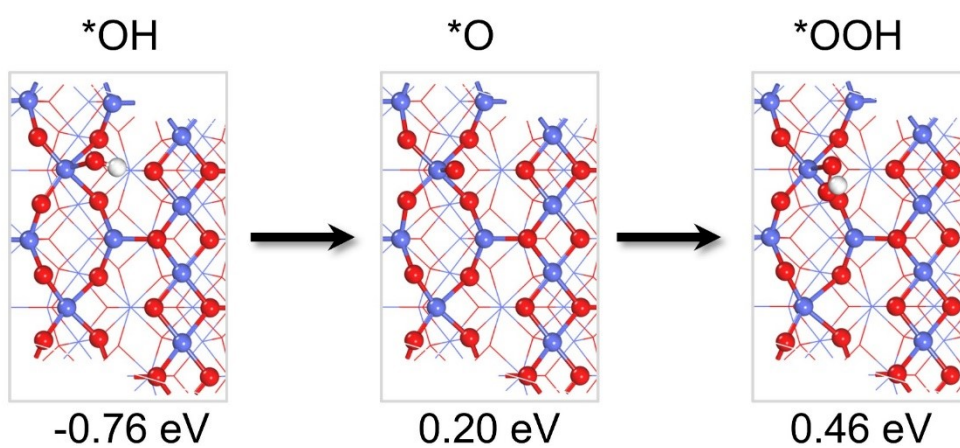
*OH   *O   *OOH

-0.76 eV   0.20 eV   0.46 eV

Figure S37. Calculated adsorption free energies of *OH, *O, and *OOH intermediates on pristine Co_3O_4 at U = 1.23 V.

*OH   *O   *OOH

-1.19 eV   -1.96 eV   -0.54 eV

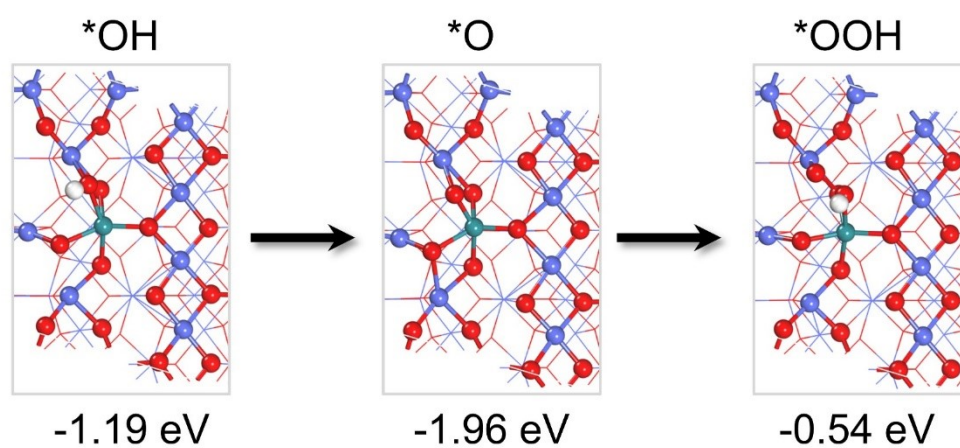**Figure S38.** Calculated adsorption free energies of *OH, *O, and *OOH intermediates on Co sites of Ru SAs-CoO$_x$ (with oxygen vacancies) at U = 1.23 V.

*OH   *O   *OOH

-1.19 eV   -2.02 eV   -0.68 eV

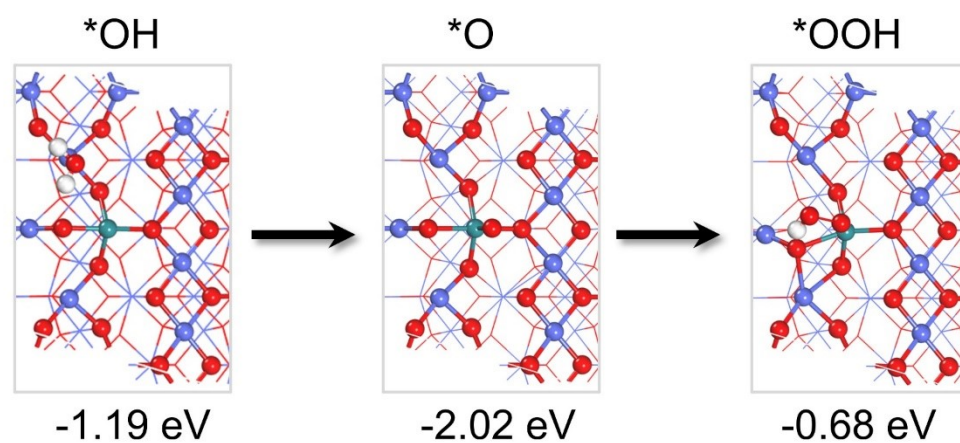**Figure S39.** Calculated adsorption free energies of *OH, *O, and *OOH intermediates on Ru sites of Ru SAs-CoO$_x$ (with oxygen vacancies) at U = 1.23 V.
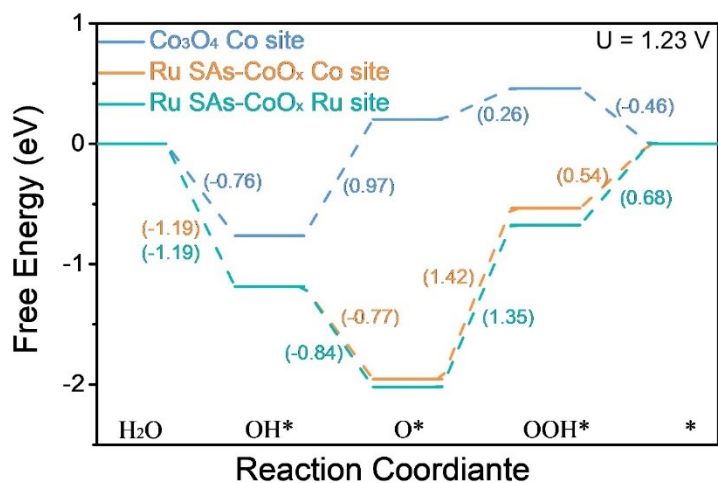
Figure S40. Calculated free energy diagrams for OER process (AEM) on different active sites.

As shown in Figure S40, the potential-determining step of the Co sites on pristine Co_3O_4 is the formation of O*, with a corresponding reaction energy is 0.97 eV. Conversely, for the Co and Ru site on Ru SAs-CoO$_x$, the potential-determining step is the formation of OOH*, with corresponding reaction energies of 1.42 and 1.35 eV, respectively. These two sites of Ru SAs-CoO$_x$ exhibit much higher energy barrier than the Co site on pristine Co_3O_4. This result is not in accordance with the boosted OER activity observed with Ru SAs-CoO$_x$.
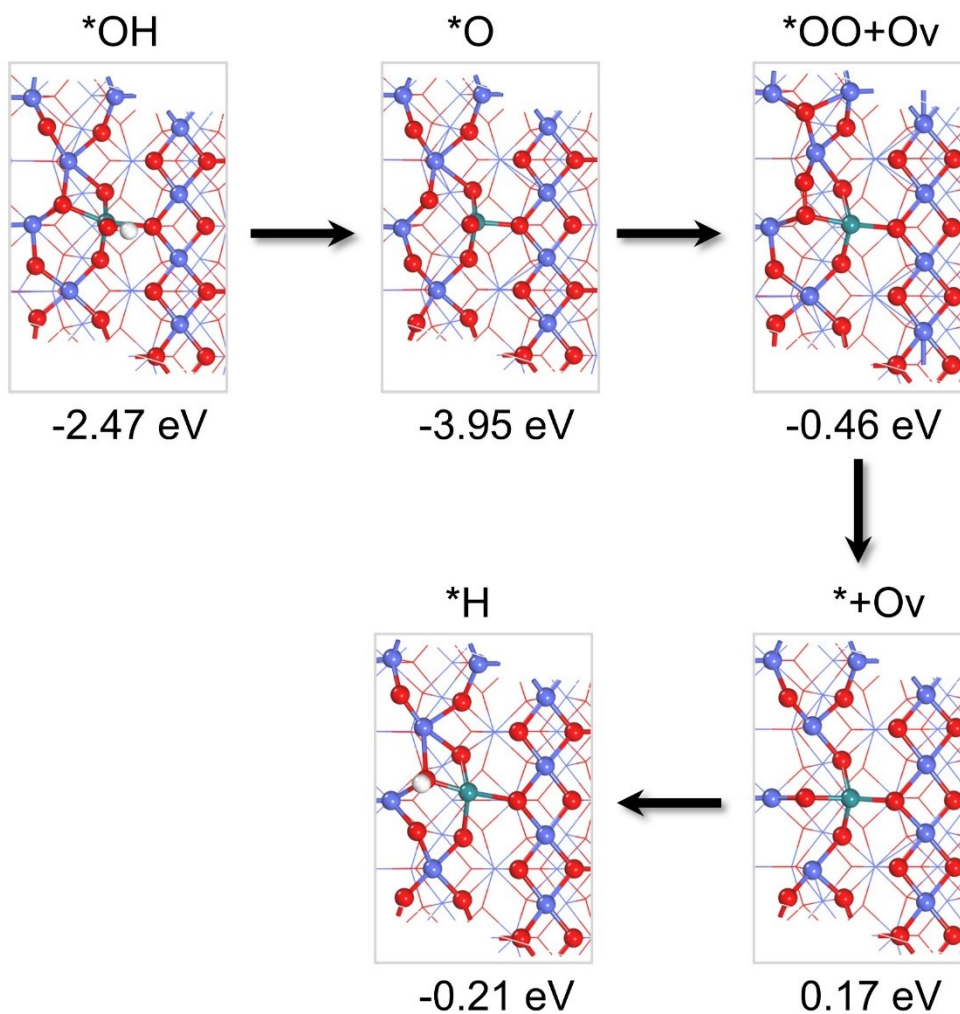

Figure S41. Calculated adsorption free energies of *OH, *O, *OO + O$_v$, *+O$_v$, *H, and * on Ru sites of Ru SAs-CoO$_x$ (without oxygen vacancies) at U = 1.23 V.
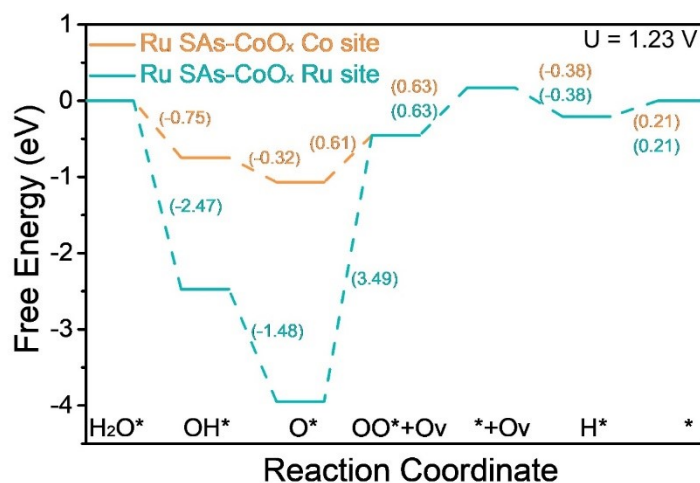
Figure S42. Calculated free energy diagrams for OER process (LOM) on different sites.
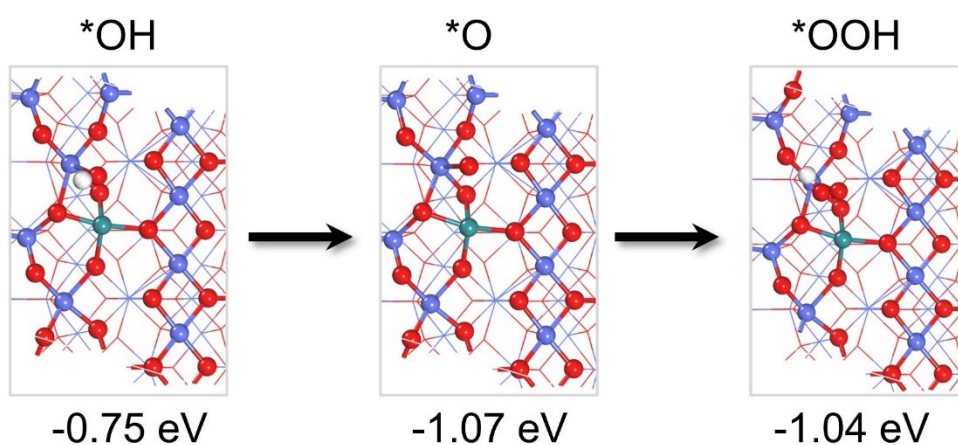
Figure S43. Calculated adsorption free energies of *OH, *O, and *OOH intermediates on Co sites of Ru SAs-CoO$_x$ (without oxygen vacancies) at U = 1.23 V.
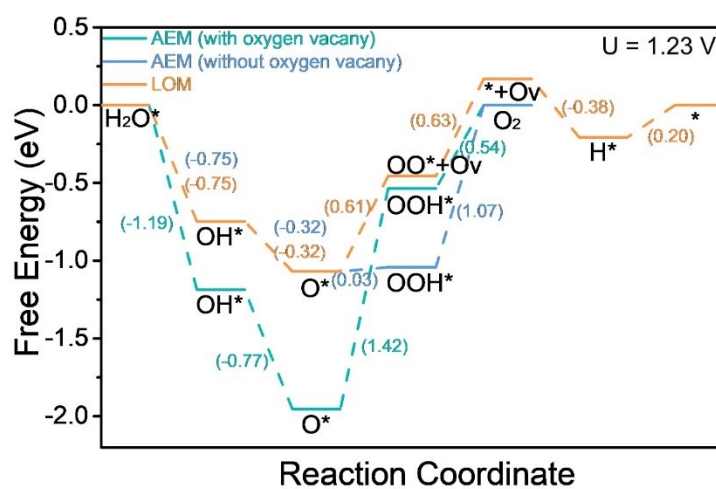
Figure S44. Calculated free energy diagrams for OER on the Co site of Ru SAs-CoO$_x$ (with/without oxygen vacancies) based on AEM and LOM.
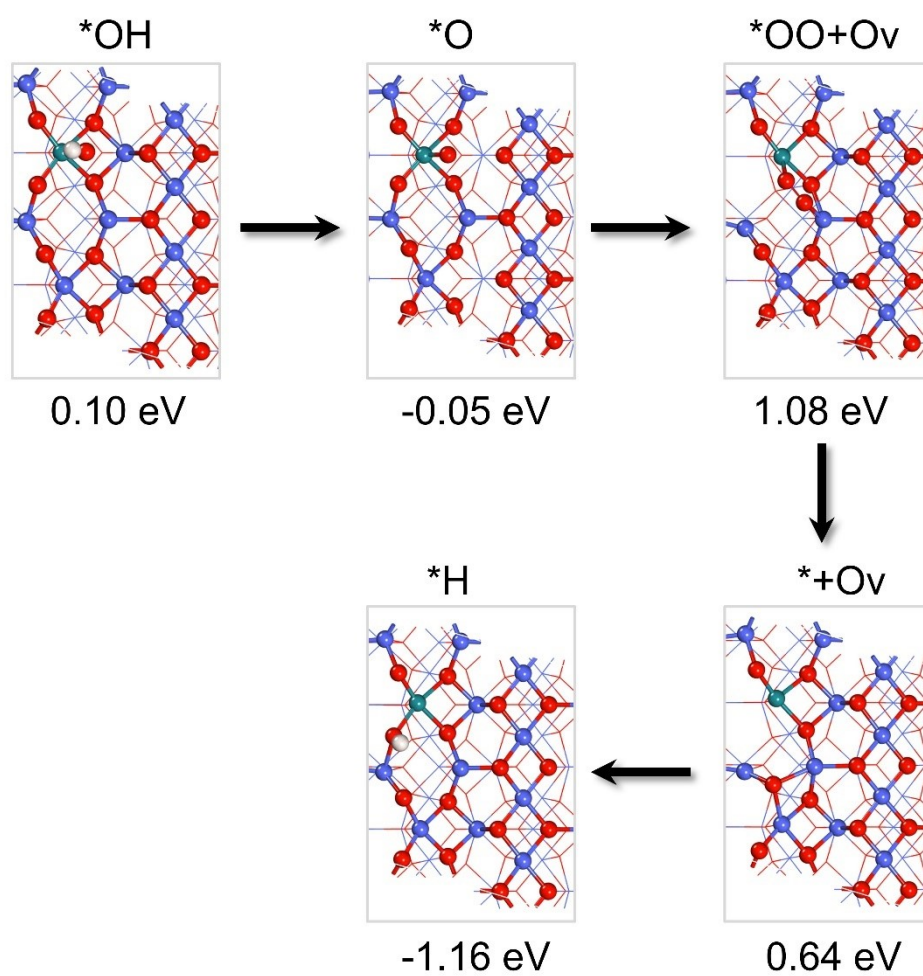
Figure S45. Calculated adsorption free energies of *OH, *O, *OO + O_v, *+O_v, *H, and * on Ru sites of Ru SAs-CoO$_x$ (with Ru replacing O_h sites) at U = 1.23 V.
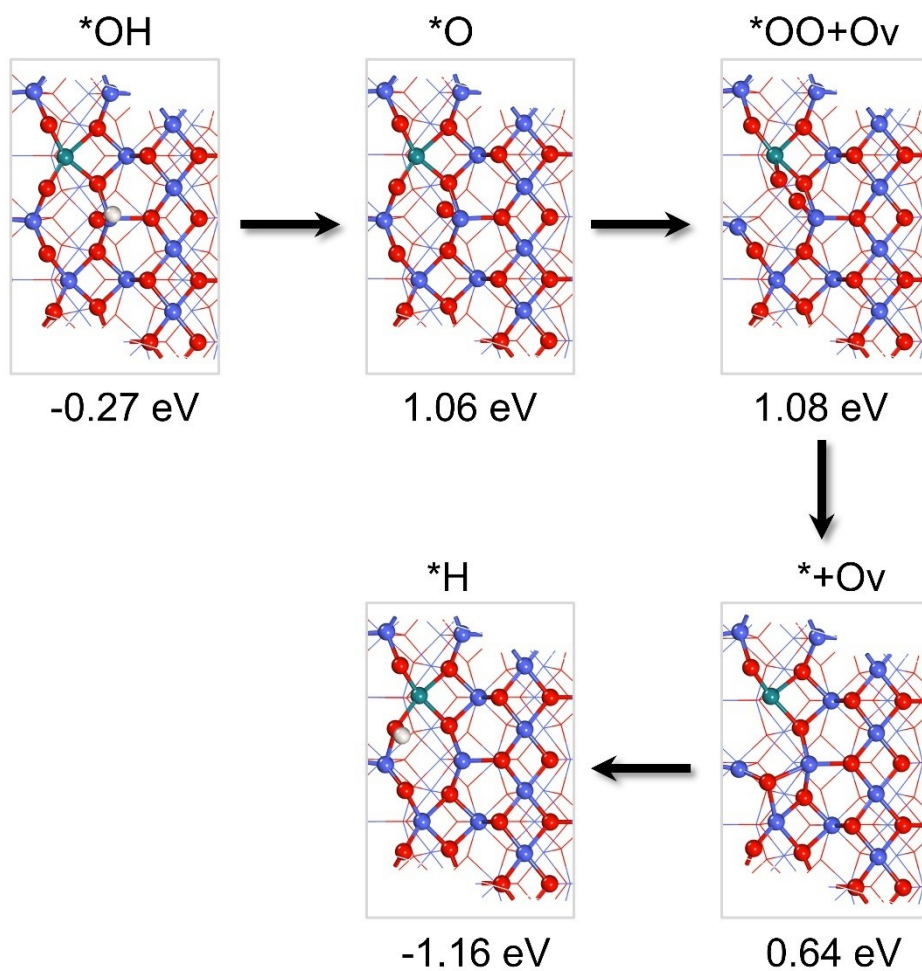
Figure S46. Calculated adsorption free energies of *OH, *O, *OO + O_v, *+O_v, *H, and * on Co sites of Ru SAs-CoO$_x$ (with Ru replacing O_h sites) at U = 1.23 V.
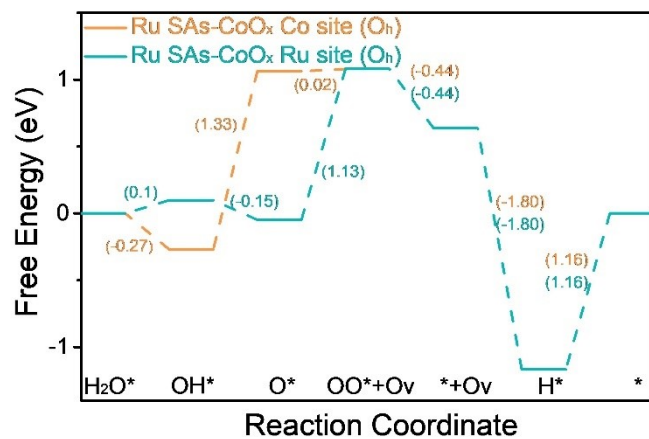
Figure S47. Calculated free energy diagrams for OER process (LOM) on different sites of Ru SAs-CoO$_x$ (with Ru replacing O_h sites).
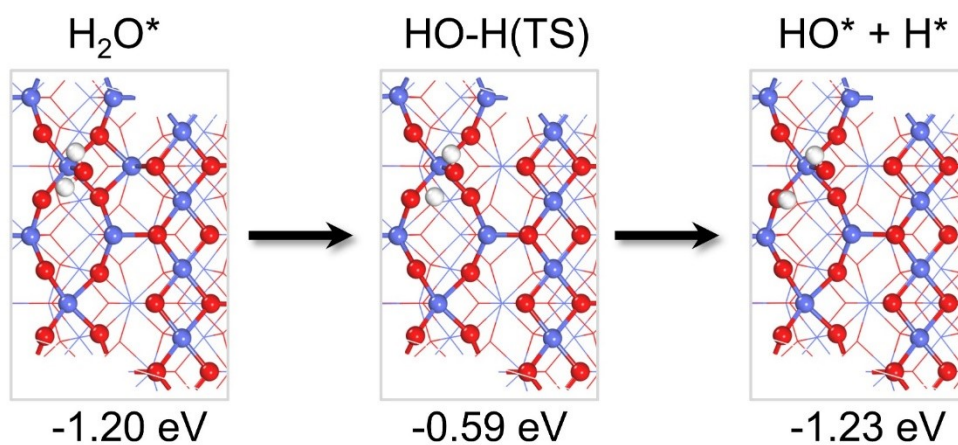
Figure S48. Calculated adsorption free energies of H_2O^*, HO-H(TS), and HO*+H* intermediates on pristine Co_3O_4 at U = 1.23 V.
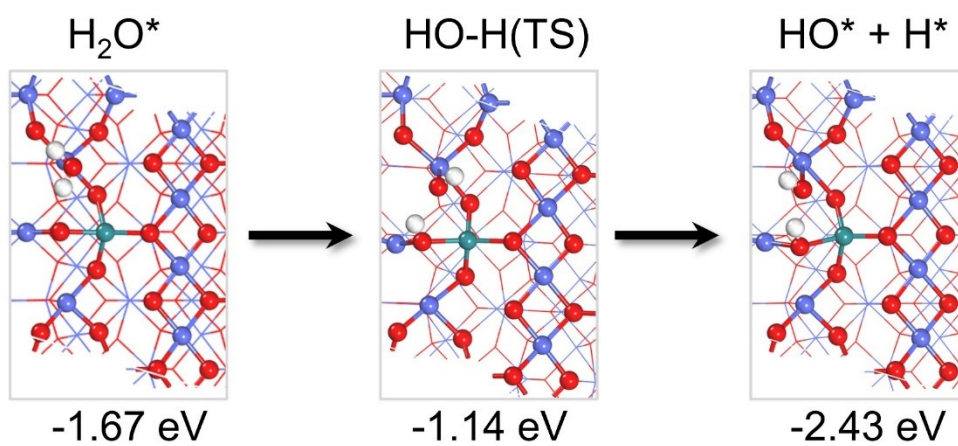
Figure S49. Calculated adsorption free energies of H_2O^*, HO-H(TS), and HO*+H* intermediates on Co site of Ru SAs-CoO$_x$ at U = 1.23 V.
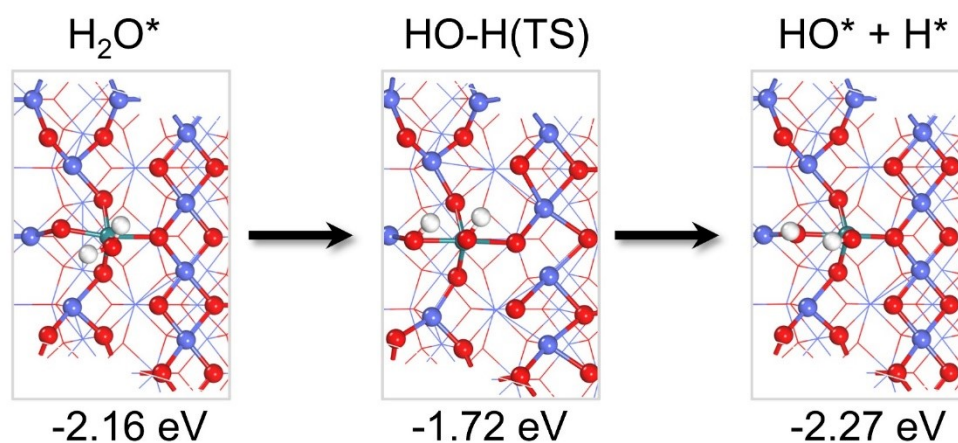
Figure S50. Calculated adsorption free energies of H_2O^*, HO-H(TS), and HO*+H* intermediates on Ru site of Ru SAs-CoO$_x$ at U = 1.23 V.

Figure S51. (a) The LSV curves of Ru SAs-CoO$_x$, Co$_3$O$_4$, and RuO$_2$ in 0.1 M HClO$_4$ with and without iR-compensation, (b) The resistance with error bar of Ru SAs-CoO$_x$, Co$_3$O$_4$, and RuO$_2$ in 0.1 M HClO$_4$. The error bars are the standard deviation from the mean (n = 3).

Table S1. Comparison of the orbital overlap between Co 3d and O 2p in the Co_3O_4, $Ru-Co_3O_4$, and $Ru-CoO_x$.

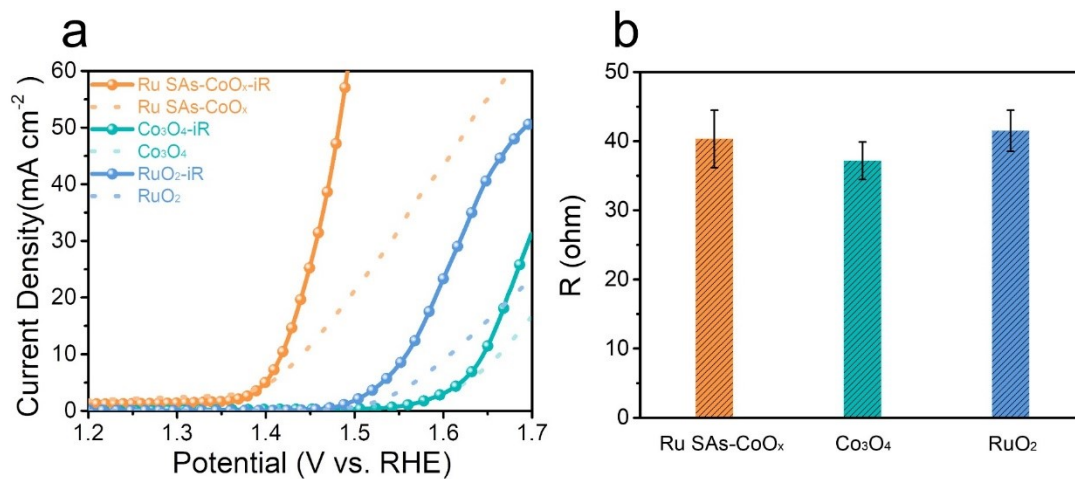|	Co 3d-band center (eV)	O 2p-band center (eV)	Co 3d – O 2p (eV)
Co_3O_4	-1.50	-1.35(O1)	-0.15
	-1.50	-2.62(O2)	1.12
$Ru-Co_3O_4$	-0.78	-0.56(O1)	-0.22
	-0.78	-1.19(O2)	0.41

Table S2. EXAFS fitting parameters at the Ru K-edge for various samples(S_0^2=0.74).

Sample	Path	CN^a	$R(Å)^b$	$\sigma^2 (Å^2)^c$	$\Delta E_0(eV)^d$	R factor (%)
Ru foil	Ru-Ru	12*	2.67±0.02	0.0038	5.30±1.80	1.1
Ru SAs-CoO$_x$	Ru-O	3.8±0.4	2.03±0.02	0.0040	-2.04±0.74	1.5
	Ru/Co-O-Co	1.2±0.3	2.68±0.02	0.0024		

$^a CN$, coordination number; $^b R$, distance between absorber and backscatter atoms; $^c \sigma^2$, Debye-Waller factor to account for both thermal and structural disorders; $^d \Delta E_0$, inner potential correction; R factor indicates the goodness of the fit. S_0^2 was fixed to 0.74, according to the experimental EXAFS fit of Ru foil by fixing CN as the known crystallographic value. Fitting range: $3.0 \leq k$ (/Å) ≤ 10.0 and $1.2 \leq R$ (Å) ≤ 2.7 (Ru SAs-CoO$_x$). A reasonable range of EXAFS fitting parameters: $0.700 < S_0^2 < 1.000$; $CN > 0$; $\sigma^2 > 0$ Å^2; $\Delta E_0 < 10$ eV; R factor < 0.02.

Table S3. ICP-AES results of different samples.

Sample	Ru (wt%)
Ru-CoO$_x$ -0.0125	3.47
Ru-CoO$_x$ -0.025	3.90
Ru-CoO$_x$ -0.05	4.39
Ru-CoO$_x$ -0.075	5.16
Ru-CoO$_x$ -0.1	6.58
Ru-CoO$_x$ -0.125	7.22

Table S4. OER activity of Ru-CoO$_x$ with different Ru content.

Sample	Overpotential / mV @ 10 mA cm^{-2}	Tafel slope / mV dec^{-1}
Ru-CoO-0.0125	231	66
Ru-CoO-0.025	224	65
Ru-CoO-0.05	212	68
Ru-CoO-0.075	188	63
Ru-CoO-0.1	192	83
Ru-CoO-0.125	217	65

Table S5. Comparison of OER performance with recently reported Ru-based and Co-based electrocatalysts in acidic media.

Catalyst	Electrolyte	Overpotential / mV @ 10 mA cm^{-2}	Tafel slope / mV dec^{-1}	Mass loading	Mass Activity	Reference
Ru SAs-CoO$_x$	0.1 M HClO$_4$	188	63	0.036 mg$_{Ru}$ cm^{-2}	2657.0 mA mg^{-1}$_{Ru}$ at 1.50 V (vs. RHE)	This work
Co-RuIr	0.1 M HClO$_4$	235	67	0.051 mg cm^{-2}	/	Adv. Mater. 2019, 31, 1900510
Ru@IrO$_x$	0.05 M H$_2$SO$_4$	282	69	1.458 mg cm^{-2}	644.8 mA mg^{-1} at 1.56 V (vs. RHE)	Chem. 2019, 5, 445
Amorphous IrO$_2$	0.1 M HClO$_4$	255	112	/	/	Nat. Commun. 2019, 10, 4855
Mn$_{0.73}$Ru$_{0.27}$O$_{2-\delta}$	0.5 M H$_2$SO$_4$	208	65	0.280 mg cm^{-2}	879.2 mA mg^{-1}$_{Ru}$ at 1.50 V (vs. RHE)	Energy Environ. Sci., 2022, 15, 2356
Ba$_2$YIrO$_6$	0.1 M HClO$_4$	318	67	0.015 mg cm^{-2}	/	Nat. Commun. 2016, 7, 12363
RuCu	0.5 M H$_2$SO$_4$	270	76	0.014 mg$_{Ru}$ cm^{-2}	800 mA mg^{-1}$_{Ru}$ at 1.50 V (vs. RHE)	ACS Appl. Energy Mater. 2019, 2, 10, 7483
Ir-STO	0.1 M HClO$_4$	295	/	0.210 mg cm^{-2}	820.0 mA mg^{-1}$_{Ir}$ at 1.50 V (vs. RHE)	Angew. Chem. Int. Ed. 2019, 58, 7631
Ru/Co-N-C-800℃	0.5 M H$_2$SO$_4$	232	68	0.400 mg cm^{-2}	15000 mA mg^{-1}$_{Ru}$ at 1.70 V (vs. RHE)	Adv. Mater. 2022, 34, 2110103

RuO$_2$/(Co,Mn)$_3$O$_4$	0.5 M H$_2$SO$_4$	270	77	/	/	*Appl. Catal. B Environ.* 2021, 297, 120442
IrRu@Te	0.5 M H$_2$SO$_4$	220	35	0.90 mg cm^{-2}	590 mA mg$^{-1}_{IrRu}$ at 1.50 V (*vs.* RHE)	*ACS Catal.* 2020, 10, 6, 3571
Au@Pt@RuO$_x$	0.1 M HClO$_4$	215	66	0.02 mg$_{Ru}$ cm^{-2}	1311.0 mA mg$^{-1}_{Ru}$ at 1.48 V (*vs.* RHE)	*J. Mater. Chem. A,* 2021, 9, 14352
RuO$_2$ NSs	0.5 M H$_2$SO$_4$	199	38	0.125 mg cm^{-2}	520 mA Ru^{-1}mg at 1.46 V (*vs.* RHE)	*Energy Environ. Sci.,* 2020, 13, 5143
Ru@Ir-O	0.5 M H$_2$SO$_4$	238	91	0.350 mg cm^{-2}	1169.0 mA mg^{-1} at 1.55 V (*vs.* RHE)	*Small* 2022, 18, 2108031
RuNi$_2$@G-250	0.5 M H$_2$SO$_4$	227	65	0.320 mg cm^{-2}	1688.8 mA cm^{-2} at 1.48 V (*vs.* RHE)	*Adv. Mater.* 2020, 32, 1908126
RuCu NSs/C	0.05 H$_2$SO$_4$	245	73	0.254 mg cm^{-2}	/	*Angew. Chem. Int. Ed.* 2019, 58, 13983

Table S6. Comparison of OER durability with recently reported Co$_3$O$_4$ electrocatalysts in acidic media.

Electrocatalyst	Durability	Reference
Ru SAs-CoO$_x$	9 mV attenuated in 25 h	This work
pristine Co$_3$O$_4$	160 mV attenuated in 2 h	This work
Co$_3$O$_4$	~200 mV attenuated in 1 h	*Nat. Commun.* 2022, 13, 7754
Co$_3$O$_4$	~100 mV attenuated in 10 h	*J. Am. Chem. Soc.* 2023, 145, 17995
Co$_3$O$_4$	~250 mV attenuated in 10 h	*Adv. Mater.* 2024, 36, 2401163
Co$_3$O$_4$	~800 mV attenuated in 8 h	*J. Mater. Chem. A,* 2024, 12, 8796

Table S7. ICP-MS data characterizing the amount of Co and Ru dissolution of Ru SAs-CoO$_x$ after 12 h and 24 h stability test.

	12 h	24 h
Co (ng)	14.5	16.8
Ru (ng)	4.8	13.7

Reference

1. J. Jin, K. Parbhakar and L. H. Dao, *Comp. Mater. Sci.* 1996, **6**, 1-6.
2. P. E. Blöchl, *Phys. Rev. B* 1994, **50**, 17953-17979.
3. J. P. Perdew, J. A. Chevary, S. H. Vosko, K. A. Jackson, M. R. Pederson, D. J. Singh and C. Fiolhais, *Phys. Rev. B* 1992, **46**, 6671-6687.
4. S. Grimme, J. Antony, S. Ehrlich and H. Krieg, *J. Chem. Phys.* 2010, **132**, 154104.
5. Z. Huang, J. Song, Y. Du, S. Xi, S. Dou, J. M. V. Nsanzimana, C. Wang, Z. J. Xu and X. Wang, *Nat. Energy* 2019, **4**, 329-338.
6. A. Grimaud, O. Diaz-Morales, B. Han, W. T. Hong, Y. Lee, L. Giordano, K. A. Stoerzinger, M. T. M. Koper and Y. Shao-Horn, *Nat. Chem.* 2017, **9**, 457-465.
7. N. Chakroune, G. Viau, S. Ammar, N. Jouini, P. Gredin, M. J. Vaulay and F. Fiévet, *New J. Chem.* 2005, **29**, 355-361.
8. A. Cao, J. Hu, H. Liang, W. Song, L. Wan, X. He, X. Gao and S. Xia, *J. Phys. Chem. B* 2006, **110**, 15858-15863.
9. L. Xu, Q. Jiang, Z. Xiao, X. Li, J. Huo, S. Wang and L. Dai, *Angew. Chem. Int. Ed.* 2016, **55**, 5277-5281.
10. J. Huang, H. Sheng, R. D. Ross, J. Han, X. Wang, B. Song and S. Jin, *Nat. Commun.* 2021, **12**, 3036.
11. Y. Li, F. Li, X. Meng, S. Li, J. Zeng and Y. Chen, *ACS Catal.* 2018, **8**, 1913-1920.